Autonomous Constrained Control of Arbitrarily-Configured Spacecraft with Broad Uncertainties

Matthew M. Wittal* and Benjamin W. Asher[†] NASA Deep Space Logistics Project Office, Kennedy Space Center, FL 32899

Morad Nazari[‡]
Embry-Riddle Aeronautical University, Daytona Beach, FL 32114

Current spacecraft control methods rely on explicit, predetermined commands, making them computationally intensive and inflexible for vehicles with mass properties and thruster configurations that change over time due to changing cargo configurations or thruster malfunctions. This work introduces a methodology within special Euclidean group SE(3) to autonomously control any spacecraft with constrained thruster configurations to enable autonomous spacecraft control under uncertainty. The approach integrates an unscented Kalman filter (UKF) on tangent bundle of SE(3), i.e. TSE(3), and a Morse-Lyapunov controller to determine optimal thruster firing sequences while overcoming state, measurement, and process uncertainties. Simulations demonstrate successful stationkeeping under randomized thruster layouts and mass distributions, successfully enabling stationkeeping for any configuration of mass properties and thrusters. Autonomous docking is successfully performed in simulations under sensor and dynamic uncertainties, including state estimation errors, measurement noise and alignment errors, and thruster misalignment. Results validate the robustness of the method in mitigating state, actuator, and sensor uncertainties, with applications to autonomous GN&C of constrained spacecraft configurations considering saturation limits.

^{*}Ph.D. Candidate, Embry-Riddle Aeronautical University, Daytona Beach, FL 32114; Lead GN&C Engineer, Deep Space Logistics, NASA Kennedy Space Center, FL 32899, matthew.m.wittal@nasa.gov

[†]Mission Design Engineer, Aegis Aerospace, NASA Kennedy Space Center, FL 32899, benjamin.w.asher@nasa.gov

[‡]Associate Professor, Aerospace Engineering Department, Embry-Riddle Aeronautical University, 1 Aerospace Blvd., Daytona Beach, FL 32114, nazarim@erau.edu

I. Nomenclature

	Latin		Greek			
\overline{c}	Thruster ontime vector	α	UKF weight			
B	Bias	β	UKF weight			
D	Deadband gain	γ	UKF weight			
d_c	Maximum ontime	ϵ	State error			
f	Force $\in \mathbb{R}^3$	η	Noise vector			
g	$Pose \in SE(3)$	θ	Euler angles $\in \mathbb{R}^3$			
\mathbb{I}	Augmented inertia $\in \mathbb{R}^{6 \times 6}$	κ	Range control gain $\in \mathbb{R}$			
J	Inertia $\in \mathbb{R}^{3\times 3}$	λ	Function of UKF weights			
${\mathcal J}$	Cost function	au	External forces and torques $\in \mathbb{R}^6$			
K	Control gain matrix	ϕ	Thruster pod angle			
k_{ij}	The j^{th} component of the i^{th} control gain	X	Vector of sigma points			
L	Torque $\in \mathbb{R}^3$	arphi	Retraction function mapping $SE(3) \rightarrow TSE(3)$			
l	Control function of relative pose	ψ	Backstepping function			
I	Length	ω	Angular rate $\in \mathbb{R}^3$			
m	Mass	ζ	Thruster clock angle			
\mathcal{N}	Normal distribution					
P	Total covariance		Latin (Cont'd)			
Q	Process Covariance	и	Control forces and torques $\in \mathbb{R}^6$			
R	Attitude \in SO(3)	\mathbb{A}	Augmented velocity $\in \mathbb{R}^6$			
r	Position $\in \mathbb{R}^3$	v	Velocity $\in \mathbb{R}^3$			
S	Control function of relative attitude	W	Weight matrix			
T	Thrust	w	Width			
U	Uniform distribution	X	State $\subset \mathbb{R}^p$			
$ ilde{U}$	Thruster mapping matrix	Y	Measurement Covariance			
	Subscripts & Superscripts		Frames			
(î)	Estimated state	\mathcal{B}^i	The <i>i</i> th body frame			
(<u>*</u>)	Unit vector $\in \mathbb{R}^3$	b^i_j	The j^{th} principal axis of the i^{th} body frame			
(7)	Average of a vector	\mathcal{G}^{J}	Geometric frame			
$(\cdot)^{\times}$	Cross map $\in \mathfrak{so}(3)$	Gi	The i^{th} principal axis of the \mathcal{G} frame			
$(\cdot)^{\vee}$	Wedge map $\in \mathfrak{so}(3)$	\mathcal{M}	actuator frame			
(\cdot)	Inverse of $(\cdot)^{\vee}$	m_{j}	The j^{th} component of the actuator frame			
·)+	Pseudo-inverse	N	Inertial frame			
·)*	Conjugate					
(·) *	Optimal value					
0	Initial value					
d	Desired state					
k	Time step					
n	Current count					
p	dimension of the measurement model					
q	dimension of the state					
•						

II. Introduction

Permanent human settlements require robust logistics for long-term sustainability. Long-duration spaceflight for a wide variety of payloads necessitates the development of autonomous spacecraft guidance, navigation and control (GN&C) tolerant to ambiguity and capable of acting independent of Earth. The Artemis program's current goal of establishing the first permanently manned colony on the surface of the Moon will necessitate the use of logistics vehicles and tugs to deliver supplies between Earth, the Gateway, and the Lunar surface. Tug-cargo spacecraft configurations are becoming increasingly popular both in low Earth orbit and for Lunar and Martian colonization ambitions from both the public and private sectors. Therefore, it is of interest to assess the controllability limitations of logistics spacecraft and develop a control framework that accounts for mass property variations, uncertain state estimation, and off-nominal configurations. This is especially challenging because the nature of logistics is such that the on-loading and off-loading of cargo necessarily changes those mass properties from one mission phase to the next. It further demands the creation of robust autonomy in spacecraft to ensure the reliable performance of these vehicles in the absence of available communication with ground stations or in the presence of rapidly changing configurations and scenarios. Future Mars missions require multi-use spacecraft with adaptable mass properties due to varying cargo configurations. Furthermore, there is an expectation that autonomy will need to be robust enough to handle off-nominal scenarios during long voyages between planets and where communication is inhibited by long light-time delays. This is especially challenging for performing Earth-independent rendezvous, proximity operations, and docking. A key step in achieving this goal is the ability of a spacecraft to autonomously determine the best use of the current thruster and mass property configuration to guide a spacecraft to the desired pose and velocity, even when there are errors in those assumptions.

While prior work has explored autonomous guidance for Entry, Descent, and Landing (EDL) [1] and thruster behavior modeling [2], these approaches typically assume nominal configurations or well-characterized mass properties. This paper extends prior work by developing an adaptive control scheme that accounts for dynamic uncertainty in mass properties, state estimation, and constrained thruster configurations. Although there are many available approaches to this challenge, Morse-Lyapunov control has become increasingly ubiquitous in academic work [3–7]. The use of Morse-Lyapunov control to solve for mass properties, track changing states, and adapt to uncertainty have recently been demonstrated within the SE(3) framework [8–10]. This strategy has also recently been applied to the multi-body problem, in unstable orbital regimes, and under constrained control [11–15].

The use of Lie group SE(3) enables GN&C algorithms to be built within this framework and enables the consideration of coupled motion even in the presence of noise without encountering the singularity or non-uniqueness issues present in other attitude parameterization sets [16–19]. In order to consider uncertainty within this framework, an unscented Kalman filters (UKF) [20–23] has recently been developed for SE(3) and its tangent bundle TSE(3) [24, 25] and has been demonstrated to be effective in the case of estimation-based controllers on SE(3) [6, 7, 9, 12, 26]. Yet despite recent work [10, 14, 27, 28], there remain challenges in implementing this controller to distributed, constrained thruster

configurations with saturation limits in the presence of uncertainty. There has been some recent work focusing on constrained control and distributed control on SE(3) and its tangent bundle TSE(3) [10, 14, 29], but these algorithms do not consider autonomous thruster firing, autonomous thruster firing histories, or duty cycle limitations which are necessary for the application of these methods to reaction control system (RCS) thrusters.

This paper presents an autonomous control methodology for spacecraft with arbitrarily configured thrusters operating under state, measurement, and actuator uncertainties. The proposed approach integrates a TSE(3)-based Unscented Kalman Filter (UKF) with a Morse-Lyapunov tracking controller to dynamically determine optimal thruster firing sequences. The simulation results demonstrate that this method enables robust spacecraft control even when thruster configurations are constrained by saturation limits, duty cycle constraints, and uncertainties in magnitude, direction, and box constraints. Importantly, the algorithm ensures full controllability across all six degrees of freedom, provided that the thruster configuration allows access to both positive and negative actuation in each direction. These capabilities are validated through two representative case studies: autonomous station-keeping of a Gateway-like platform under dynamic disturbances and a fully autonomous rendezvous, proximity operations, and docking (RPOD) maneuver under significant sensor uncertainties.

Standard optimization-based control methods struggle with constrained thruster configurations due to their reliance on continuous inputs, assumptions of convex constraints, and computational complexity [1, 30, 31]. These methods are often fail or are not applied because (1) they assume continuously adjustable control inputs, while thrusters operate in discrete on-off cycles; (2) they struggle with nonlinear actuator constraints like saturation limits and duty cycles; (3) they can lead to excessive thruster chattering, increasing fuel consumption and actuator wear; and (4) they may require excessive computation time, making real-time control impractical. To address these issues, this paper introduces a constraint-enforced control approach that enforces duty cycle constraints while ensuring feasible thruster activations in real time. This approach has been validated using a medium-fidelity spacecraft and sensor model based on the Gateway logistics module.

Following this introduction, this paper is divided into six more sections. Section III introduces the special Euclidean group SE(3) and its tangent bundle TSE(3) and describes relative pose dynamics, the TSE(3)-based UKF, and the estimation-based Morse-Lyapunov tracking controller used in this work, all of which are foundational aspects of this paper and have been the topics of previously published articles. Next, Section V describes the methodology for taking the desired control input about the body frame from the Morse-Lyapunov controller, distributing it to arbitrary, constrained configuration of thrusters, and imposing saturation limits driven by thruster limitations and bounded by the maximum duty cycle. This methodology is applied in Section VI where two scenarios are explored: one of the Gateway with randomly generated thruster configurations and mass properties maintains its position in the presence of significant but acute disturbances, and a second where a logistics vehicle with a constrained thruster configuration autonomously docks with a stationary Gateway. In the second scenario, robust uncertainty is introduced including ambiguity in state,

measurements, sensor orientation and position, thruster orientation and position, thruster magnitude, and process noise. Conclusions based on these findings are discussed in Section VII.

III. Preliminaries

The Lie group SE(3) is a convenient formulation for scenarios in which translational and rotational motion are coupled. Some examples of this include solar radiation pressure (SRP), gravity gradient torques, relative motion, and proximity operations. Traditional methods of having separate control strategies for both translational and rotational motion require additional considerations that add complexity to a guidance and control scheme, while for SE(3) and its sister formulation dual quaternions only two lines are needed to capture the differential states for any give time step. In this section, these dynamics, relevant reference frames, and error dynamics within this framework are introduced and defined.

A. Dynamics on TSE(3)

The pose (i.e. orbital position and attitude), of a rigid-body is represented using the SE(3) transformation matrix as

$$g =: \begin{bmatrix} R & r \\ 0_{1 \times 3} & 1 \end{bmatrix} \in SE(3) \tag{1}$$

where $R \in SO(3)$ is the rotation matrix from a rigid body frame \mathcal{B} to some inertial frame \mathcal{N} and r is the position vector of the center of mass with respect to and expressed in that inertial frame. The smoothness of the matrix Lie group implies the existence of a single tangent space at each point. The tangent space at the identity element of the group is referred to as Lie algebra [32] and is denoted as

$$\mathfrak{se}(3) = \left\{ \mathbb{V}^{\vee} = \begin{bmatrix} \omega^{\times} & v \\ 0_{1\times 3} & 0 \end{bmatrix}, \ \omega^{\times} \in \mathfrak{so}(3), \ v \in \mathbb{R}^{3} \right\}$$
 (2)

where $(\cdot)^{\vee}$ indicates the wedge map, i.e. $(\cdot)^{\vee}: \mathbb{R}^6 \to \mathfrak{se}(3)$ applied to the vector $\mathbb{V} = [\omega^T, v^T]^T$ which is the augmented velocity vector, defined through the translational velocity $v \in \mathbb{R}^3$ and the angular velocity $\omega \in \mathbb{R}^3$; $\mathfrak{so}(3)$ is the set of 3 by 3 skew-symmetric matrices defined under the cross-map $(\cdot)^{\times}: \mathbb{R}^3 \to \mathfrak{so}(3)$ so that for the vector $\omega = [\omega_1, \omega_2, \omega_3]^T$,

$$\omega^{\times} = \begin{bmatrix} 0 & -\omega_3 & \omega_2 \\ \omega_3 & 0 & -\omega_1 \\ -\omega_2 & \omega_1 & 0 \end{bmatrix}$$
 (3)

The rigid body's augmented velocity vector is

$$\mathbb{V} = \left[\omega^T, v^T\right]^T \in \mathbb{R}^6 \tag{4}$$

It can be shown that the dynamic equations for a rigid body with an be expressed in TSE(3) as

$$\dot{g} = g \mathbb{V}^{\vee} \tag{5a}$$

$$\dot{\mathbb{V}} = \mathbb{I}^{-1} \left(\operatorname{ad}_{\mathbb{V}}^* \mathbb{I} \mathbb{V} + \tau + u \right) \tag{5b}$$

where $\tau = [L^T, f^T]^T \in \mathbb{R}^6$ represents the impressed dynamics acting on the system, with $L \in \mathbb{R}^3$ and $f \in \mathbb{R}^3$ representing all external torques and forces, respectively, both expressed in the \mathcal{B} frame. Furthermore, the augmented vector of control inputs is given by $u = \begin{bmatrix} u_L^T, u_f^T \end{bmatrix}^T \in \mathbb{R}^6$, where $u_L \in \mathbb{R}^3$ and $u_f \in \mathbb{R}^3$ represent control torques and forces, respectively. The augmented inertia tensor \mathbb{I} is defined as

$$\mathbb{I} = \begin{bmatrix} J & 0_{3\times3} \\ 0_{3\times3} & mI_3 \end{bmatrix} \in \mathbb{R}^{6\times6},$$
(6)

where $J \in \mathbb{R}^{3 \times 3}$ is the inertia matrix about the center of mass and $m \in \mathbb{R}$ is the mass of the body. The co-adjoint operator is defined as

$$\operatorname{ad}_{\mathbb{V}}^{*} = \operatorname{ad}_{\mathbb{V}}^{T} = \begin{bmatrix} -\omega^{\times} & -\nu^{\times} \\ 0_{3\times 3} & -\omega^{\times} \end{bmatrix} \in \mathbb{R}^{6\times 6}, \tag{7}$$

where

$$ad_{\mathbb{V}} = \begin{bmatrix} \omega^{\times} & 0_{3\times 3} \\ v^{\times} & \omega^{\times} \end{bmatrix} \in \mathbb{R}^{6\times 6}$$
(8)

which is used in the dynamics of a rigid body to map the angular and translational velocity simultaneously.

B. Reference Frames

As illustrated in Fig. 1, several reference frames are used in this paper. The chaser body frame, denoted by \mathcal{B}^1 , is most commonly used. In addition, the target body frame \mathcal{B}^2 is likewise significant, especially in the numerical simulation and results sections. The geometric frame \mathcal{G} is used to refer to a fixed point on the spacecraft, usually at a docking interface. The n^{th} motor frame \mathcal{M}_n refers to the given pose of an actuator and is usually expressed relative to the geometric or body frame and has a thrust component in its own frame $T_{\mathcal{M},n}$. A common inertial frame, \mathcal{N} , is used as a medium for propagating dynamics.

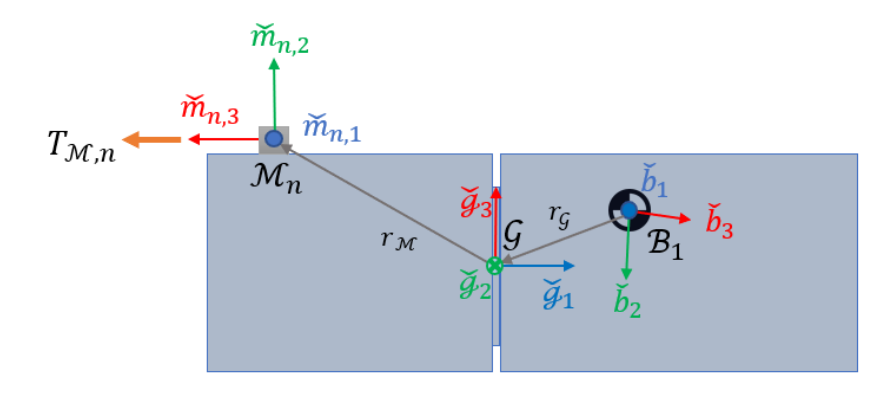


Fig. 1 An illustration of the terminology associated with various frames within the spacecraft configuration.

Each of these frames are be expressed in terms of its basis function \check{b}_1^1 , \check{b}_2^1 , \check{b}_3^1 , which represent the x-, y-, and z-components of the chaser body frame, in this case. The expression of one frame relative to another, for example the \mathcal{B}^1 frame relative to the \mathcal{N} , is expressed generally as ${}^{\mathcal{N}}R_{\mathcal{B}^1}$. Using this notation, it becomes easy to understand the appropriate application of rotation matrices. For example, the attitude of \mathcal{B}^1 with respect to \mathcal{B}^2 using some common reference frame \mathcal{N} is ${}^{\mathcal{B}^2}R_{\mathcal{B}^1}={}^{\mathcal{B}^1}R_{\mathcal{N}}{}^{\mathcal{N}}R_{\mathcal{B}^1}={}^{\mathcal{N}}R_{\mathcal{B}^1}{}^{\mathcal{N}}R_{\mathcal{B}^1}$, such that the \mathcal{N} frame superscript and subscript are "canceled out".

Finally, there exists a distinction between the estimated pose \hat{g} and the desired pose g_d . These represent two often very slightly different values of the same frame. In most cases, they are only used in the expression of error dynamics, elaborated upon in the next section. However, it is useful to think of these as their own frames, as the same mathematics used below can apply both to error dynamics and tracking between two distinct frames or rigid bodies. Expressing one pose relative to another using the same example is denoted as $g_{\mathcal{M}/\mathcal{B}}$, and an error between the desired and measured poses is denoted using ϵ_g .

C. Error Dynamics

In applied GN&C, the true states of any vehicle are unknowable and corrupted by noise, bias, uncertainty, and compounded by human and mechanical failures. Thus, in the context of error dynamics, the objective of the control system is to track a reference state based on and relative to the current, estimated state. As with any real-world scenario, the stability of any controller depends on a good understanding of the system's noise properties under nominal operations. However, since the objective of this work is to demonstrate that the described control methodology is capable of overcoming a wide variety of noise sources of conservatively high magnitude, it is assumed that broad uncertainty exists, and that the sources of noise are not well understood. In the work described herein, two sources of error are assumed: Estimation error defined by $\hat{e} = x - \hat{x}$ and tracking error defined as $e_d = x - x_d$, where x is a generalized true state or parameter, \hat{x} is the estimated state or parameter, and x_d is the desired state or parameter. The difference between

these errors can be expressed as $\epsilon_x = \hat{e} - e_d = x_d - \hat{x}$, thus illustrating that the true state is not needed in equations that express the relative state or parameters between estimated and desired elements, and that asymptotic stability about the tracked or desired state is achievable. This is defined within SE(3) and expressed as the relative pose between the estimated and desired state, i.e.

$$\epsilon_{g} = g_{d}^{-1} \hat{g} = \begin{bmatrix} R_{d} & \epsilon_{r} \\ 0 & 1 \end{bmatrix} = \begin{bmatrix} R_{d}^{T} \hat{R} & R_{d}^{T} (\hat{r} - r_{d}) \\ 0 & 1 \end{bmatrix} \in SE(3)$$

$$\epsilon_{\mathbb{V}} = \hat{\mathbb{V}} - Ad_{\epsilon_{g}} \mathbb{V}_{d} \in \mathbb{R}^{6}$$
(9)

where the subscript 'd' denotes the desired or modeled state or parameter. Eq. (10) describes state error propagation and is analogous to Eq. (5) but for error dynamics. The relative dynamics of a rigid body in SE(3) are represented as

$$\dot{\epsilon}_g = \epsilon_g \epsilon_{\mathbb{V}}^{\vee} \tag{10a}$$

$$\dot{\epsilon}_{\mathbb{V}} = \frac{d}{dt} \left(\hat{\mathbb{V}} - \operatorname{Ad}_{\epsilon_g} \mathbb{V}_d \right) = \dot{\hat{\mathbb{V}}} - \operatorname{ad}_{\epsilon_{\mathbb{V}}} \operatorname{Ad}_{\epsilon_g} \mathbb{V}_d - \operatorname{Ad}_{\epsilon_g^{-1}} \dot{\mathbb{V}}_d$$
 (10b)

Consider an actuator $g_{\mathcal{M}} \in SE(3)$ where \mathcal{M} denotes the frame of a motor or actuator with respect to the rigid body. This frame has a pose defined as

$$g_{\mathcal{M}} = \begin{bmatrix} M_{R_{\mathcal{B}}} & r_{\mathcal{M}} \\ 0_{1\times 3} & 1 \end{bmatrix} \in SE(3)$$
 (11)

where $r_{\mathcal{M}}$ is the position of the body with respect to the thruster. The relative motion dynamics expressed above are extended to describe the pose of a thruster relative to a central body in either a geometric frame \mathcal{G} , which is advantageous for unknown or arbitrary mass properties, or relative to a standard body frame \mathcal{B} , which is centered about the center of mass and oriented to ensure that the inertia tensor J is in a diagonal form. This is expressed in this work as ${}^{\mathcal{M}}g_{\mathcal{G}}$ or ${}^{\mathcal{M}}g_{\mathcal{B}}$, respectively, as illustrated in Fig. 1. The linear adjoint operator of this relative configuration is derived as follows:

$$Ad_{g_{\mathcal{M}}} = \begin{bmatrix} \mathcal{M}_{R_{\mathcal{B}}} & 0_{3\times 3} \\ r_{\mathcal{M}}^{\times} \mathcal{M}_{R_{\mathcal{B}}} & \mathcal{M}_{R_{\mathcal{B}}} \end{bmatrix} \in \mathbb{R}^{6\times 6}$$
(12)

This adjoint operation is performed on the inverse of the pose and transposed to yield the useful expression

$$\operatorname{Ad}_{g_{\mathcal{M}}^{-1}}^{T} = \begin{bmatrix} R_{\mathcal{B}/\mathcal{M}} & {}^{\mathcal{M}}R_{\mathcal{B}} \left({}^{\mathcal{M}}R_{\mathcal{B}}^{T}r_{\mathcal{M}}\right)^{\times} \\ 0_{3\times3} & {}^{\mathcal{M}}R_{\mathcal{B}} \end{bmatrix} \in \mathbb{R}^{6\times6}$$
(13)

However, an intermediate frame \mathcal{G} is defined to represent the geometric frame, defined at some fixed point on the rigid body $r_{\mathcal{G}}$ relative to the body frame \mathcal{B} . When considering a logistics spacecraft, defining this frame about the docking adapter is convenient. The relative adjoint between two frames can be expanded as the product of two relative frames as

$$\operatorname{Ad}_{g_{\mathcal{M}/\mathcal{B}}^{-1}}^{T} = \begin{bmatrix} M_{R_{\mathcal{G}}} & M_{R_{\mathcal{G}}} \left(M_{R_{\mathcal{G}}^{T} r_{\mathcal{M}}} \right)^{\times} \\ 0_{3 \times 3} & M_{R_{\mathcal{G}}} \end{bmatrix} \begin{bmatrix} \mathcal{G}_{R_{\mathcal{B}}} & \mathcal{G}_{R_{\mathcal{B}}} \left(\mathcal{G}_{R_{\mathcal{B}}^{T} r_{\mathcal{G}}} \right)^{\times} \\ 0_{3 \times 3} & \mathcal{G}_{R_{\mathcal{B}}} \end{bmatrix} = \operatorname{Ad}_{g_{\mathcal{M}/\mathcal{G}}^{-1}}^{T} \operatorname{Ad}_{g_{\mathcal{G}/\mathcal{B}}^{-1}}^{T}$$

$$(14)$$

These frame transformations are useful not just from one rigid body frame to another, but also between an estimated frame and a desired frame, as shown in Eq. (10b). The same method may be applied to examine error between the estimated and true frame, or true frame and desired frame, or any combination thereof. In the next section, these relative dynamics become important in the formulation and application of estimation-based tracking control, for where the method of Morse-Lyapunov controller design is employed.

In this paper, the formulation covered in [24, 33] is used to accommodate a stochastic process in the model. Since the source of noise is assumed to be in vector space, the exponential map $\exp(\cdot)$ is used to map it into SE(3) as

$$\hat{g} = g \exp(\eta_g^{\vee}) \quad \eta_g \sim \mathcal{N}(0_{p \times 1}, Q_g)$$
(15)

where $\hat{g} \in SE(3)$ is the noisy, estimated pose, $g \in SE(3)$ is the true pose, and $\eta_g \in \mathbb{R}^6$ denotes the pose process noise in Euclidean space with a zero mean Gaussian distribution. Note that the exponential mapping of η_g onto the estimated pose \hat{g} is multiplicative, as shown in Eq. (15). Also note that calculation of the maximum likelihood estimate (MLE) should be performed within the Euclidean space in which the noise is defined, not in the Lie group or Lie algebra.

It is assumed that the rigid body pose and augmented velocity are measurable and the output of the system, $y \in \mathbb{R}^q$ consists of the Euler angles, the translational vector components r, the angular velocity ω , and the translational velocity v. It must be emphasized that Euler angles are only used to represent the attitude in the simulation results, while they are obtained based on the rotation matrix. This produces a compact, stochastic system formulation on TSE(3) as

$$\dot{\hat{x}} : \begin{cases} \dot{\hat{g}} = g \mathbb{V}^{\vee} \exp(\eta_g^{\vee}) \\ \dot{\hat{\mathbb{V}}} = \mathbb{I}^{-1} \operatorname{ad}_{\mathbb{V} + \eta_{\mathbb{V}}}^* \mathbb{I}(\mathbb{V} + \eta_{\mathbb{V}}) + \mathbb{I}^{-1} u \end{cases}$$
(16)

$$y = \left[\left(\log_{\mathsf{SF}(3)} (\exp(\zeta_g)g)^{|} \right)^T, \, \mathbb{V}^T + \zeta_{\mathbb{V}}^T \right]^T \in \mathbb{R}^q$$
 (17)

where $(\cdot)^{\parallel}$ is the inverse of the wedge map. The dependence on time is omitted for the readability of the equations. The state process noise $\eta = [\eta_g^T, \eta_{\mathbb{V}}^T]^T \in \mathbb{R}^p$ is assumed to be a Gaussian white noise with zero mean and covariance matrix $Q \in \mathbb{R}^{p \times p}$, i.e. $\eta \sim \mathcal{N}(0_{p \times 1}, Q)$, and the measurement noise $\zeta = [\zeta_g^T, \zeta_{\mathbb{V}}^T]^T \in \mathbb{R}^q$ is assumed to be a Gaussian white noise with zero mean and covariance matrix $Y \in \mathbb{R}^{q \times q}$, i.e. $\zeta \sim \mathcal{N}(0_{q \times 1}, T)$. Furthermore, the process noise and measurement noise are assumed to be uncorrelated. The process noise given in Eq. (15) includes components for both \hat{g} and $\hat{\mathbb{V}}$ in the form of the process noise η .

IV. Estimation-Based Morse-Lyapunov Tracking Control on TSE(3)

Although the approach described in this work is agnostic to the method of generating control, using a coupled controller aligns well with the SE(3) formulation. Alternative coupled controllers, such as sliding mode control, could also be suitable for this application. The Morse-Lyapunov controller is selected due to its demonstrated capability to address mass property ambiguities, particularly when extended to state-and-parameter-error-based tracking control [26]. Although this approach is not fuel-optimal, it is designed for rapid convergence and effectively mitigates issues related to unwinding and singularities. However, one can approach fuel optimality by tuning the deadband gains described in Section V.

A. State Estimation using a UKF on TSE(3)

Similar to other Kalman filters, the UKF on SE(3), illustrated in Fig. 2, begins by taking initial state estimates $\hat{x}_{k|k}$ and a total state covariance $P_{k|k} \in \mathbb{R}^{p \times p}$ where p is the number of state variables. In this work, the state vector $\hat{x} \equiv (g, \mathbb{V}) \in \mathsf{TSE}(3)$. An initial guess is propagated to generate an a priori state estimate, $\hat{x}_{k+1|k}$, using some nonlinear dynamical function $f(x, \eta_p)$, where $\eta_p \in \mathbb{R}^p$ is the process noise with a process noise covariance Q. The UKF uses sigma points serve as small perturbations to $\hat{x}_{k+1|k}$ to compute an updated covariance $P_{k+1|k}$. The sigma points are structured in the matrix $\chi_p \in \mathbb{R}^{p \times (2p+1)}$ of 2p+1 sigma-point column vectors $\chi_{p,i}$ and the matrix $\chi_q \in \mathbb{R}^{q \times (2q+1)}$ of 2q+1 sigma column vectors $\chi_{q,i}$. Additionally, the weight matrices are defined as

$$W_p^{(m)} = [W_{p,0}^{(m)}, W_{p,1}^{(m)}, \cdots, W_{p,4p}^{(m)}]$$

$$W_p^{(c)} = [W_{p,0}^{(c)}, W_{p,1}^{(c)}, \cdots, W_{p,4p}^{(c)}]$$
(18)

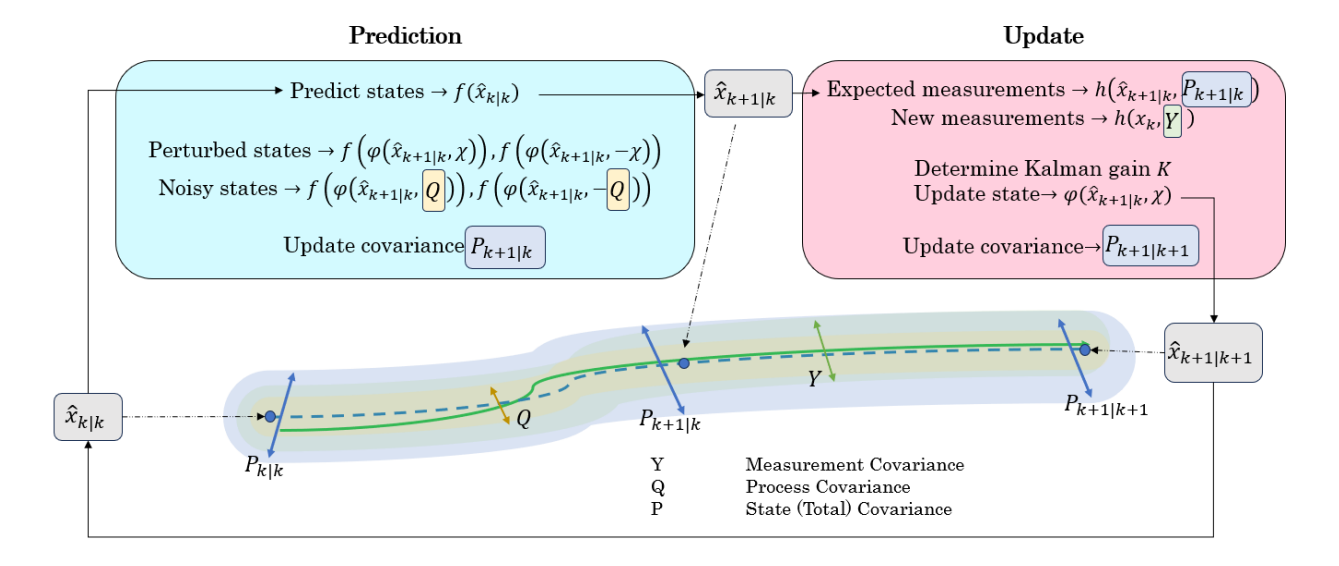


Fig. 2 An illustration of the methodology behind the UKF on TSE(3)

where

$$W_{p,0}^{(m)} = \frac{\lambda_p}{\lambda_p + p}, \quad W_{p,0}^{(c)} = \frac{\lambda_p}{\lambda_p + p} + (1 - \alpha^2 + \beta)$$

$$W_{p,i}^{(m)} = W_{p,i}^{(c)} = \frac{1}{2(\lambda_p + p)} \qquad (i = 1, 2, \dots, 4p)$$
(19)

This same procedure is repeated for $W_q^{(m)}$ and $W_q^{(c)}$ with corresponding parameter $\lambda_q = (\alpha^2 - 1)q$ instead of $\lambda_p = (\alpha^2 - 1)p$. Since the sigma points are evaluated in Euclidean space but the states of the system x evolve in TSE(3), designing the UKF on SE(3) requires a set of retractions and mappings between nonlinear manifold and the Euclidean space for both sigma points and states. Noise is defined within the Lie algebra, whereas state propagation occurs in TSE(3) [24, 25]. Since the nonlinear manifold of rigid body motion group SE(3) is a semidirect product of SO(3) and \mathbb{R}^6 , i.e. SE(3) = SO(3) × \mathbb{R}^6 , it forms a smooth manifold. Therefore, any dynamical system containing at least a rigid body subsystem, there exists a neighborhood $x \in TSE(3) \times \mathbb{R}^{12}$ that is diffeomorphic to an open subset $X \in \mathbb{R}^{12}$. The true dynamics are then propagated using a variational integrator, first introduced by [16], which advances the initial states x_k to g_{k+1} and \mathbb{V}_{k+1} . These newly generated states are passed through a measurement model $h(x_{k+1}, \eta_m) \in \mathbb{R}^q$ where $\eta_m \in \mathbb{R}^q$ is the measurement noise and q is the dimension of the measurement model and $Y \in \mathbb{R}^q$ is the measurement model covariance. If all states are observable, then p = q. The newly measured state is then used to compute an updated Kalman gain, which in turn updates the a priori state estimates to the a posteriori state estimates in the update step as $\hat{x}_{k+1|k} \to \hat{x}_{k+1|k+1}$. Finally, the a posteriori error covariance matrix is computed as

$$P_{k+1|k+1} = P_{k+1|k} - K_{k+1} P_{zz,k+1} K_{k+1}^{T}$$
(20)

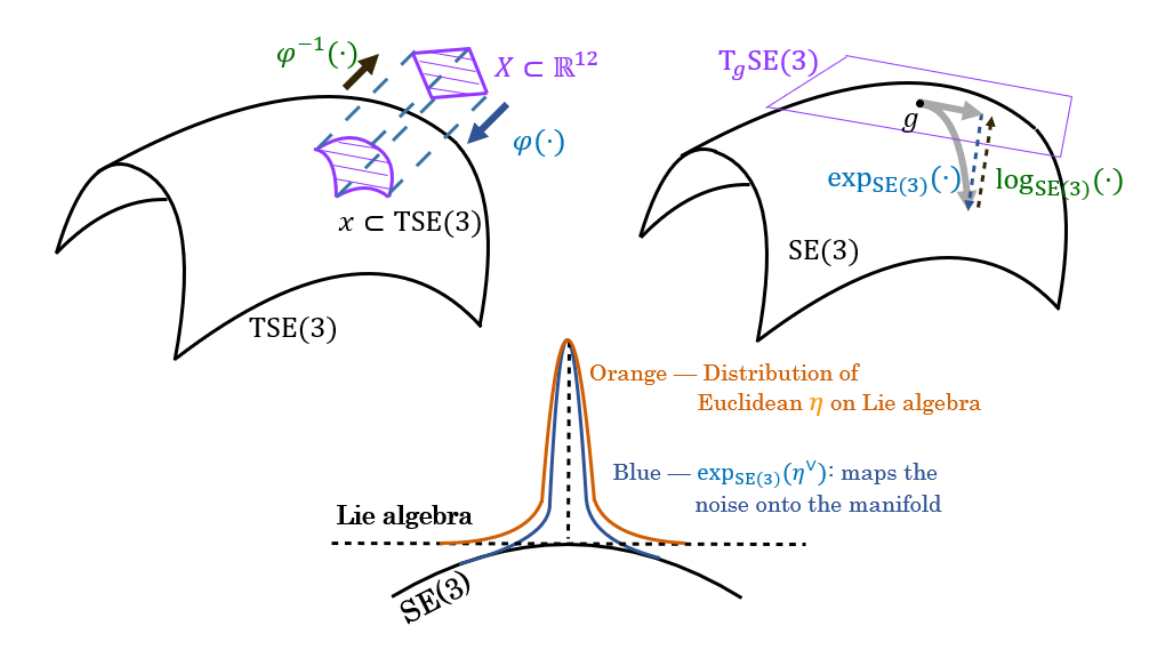


Fig. 3 An illustration of the retraction mapping between SE(3) and TSE(3)

A comprehensive discussion on the implementation details of the TSE(3)-based UKF, including its derivation and specific computational steps, is available in [9]. The UKF on SE(3) originally introduced by [24] and extended to the application of tracking control by [9] is employed in this work. The fundamental component of this UKF is the retraction function, as illustrated in Fig. 3. This function enables filtering directly on the manifold by mapping the sigma points in Euclidean space onto the nonlinear manifold, allowing for an accurate representation of system dynamics while avoiding singularities inherent to traditional parameterizations. The state illustrated by $X \in \mathbb{R}^{12}$ in Fig. 3 is mapped to TSE(3) = $\mathbb{R}^6 \times SE(3)$ using the retraction function φ , defined as

$$\varphi(x,\chi_i): \begin{cases} \varphi_g = g \exp(\chi_{g,i}^{\vee}) \\ \varphi_{\mathbb{V}} = \mathbb{V} + \operatorname{Ad}_{\chi_g} \chi_{\mathbb{V},i} \end{cases}$$
 (21)

and where it is defined as $x \in TSE(3)$. It can be mapped back to SE(3) using the inverse of the retraction function φ^{-1} defined as

$$\varphi^{-1}(\hat{x}, x) : \begin{cases} \varphi_g^{-1} = \log_{\mathsf{SE}(3)}(\hat{g}^{-1}g) \\ \varphi_{\mathbb{V}}^{-1} = \hat{\mathbb{V}} - \mathsf{Ad}_g \mathbb{V} \end{cases}$$
 (22)

We use this property to create a smooth retraction mapping $\varphi: X \to x$ which is a diffeomorphism between X and x. The logarithmic mapping $\log_{\mathsf{SE}(3)}(\cdot)$ from $\mathsf{TSE}(3)$ to $\mathsf{SE}(3)$ is leveraged for the acquisition of the deviations applied to the exponential coordinates. That is, this mapping and its inverse, which use exponential and logarithmic

functions based on SE(3), encode the UT sigma points corresponding to process and measurement noise on the manifold and decode them from the manifold, respectively (see Fig. 3). For instance, for a single rigid body with states $x \equiv (g, \mathbb{V}) \in \mathsf{TSE}(3)$, the retraction is of a form like $\varphi(\hat{x}, \chi_x) = (\hat{g} \exp_{\mathsf{SE}(3)}(\chi_g^\vee), \chi_{\mathbb{V}} + \mathsf{Ad}_g \hat{\mathbb{V}}) \in \mathsf{TSE}(3)$, where \hat{x} is the estimate of vectorized states including the exponential coordinates associated with the pose, $\chi_x = [\chi_g^T, \chi_{\mathbb{V}}^T]^T$ denotes the Euclidean sigma point vectors associated with pose and velocity, and the Adjoint transformation "Ad $_g$ " is well defined in the literature [6, 34–36]. The inverse of retraction decodes the sigma points in a form like $\varphi^{-1}(\hat{x}) = [(\log_{\mathsf{SE}(3)}(\hat{g}_0^{-1}\varphi_{g_0}))^{|T}, (\varphi_{\mathbb{V}_0} - \mathsf{Ad}_{g_0}\hat{\mathbb{V}}_0)^T]^T \in \mathbb{R}^p$. In this work, the simplest case of p = 12 is used.

B. Morse-Lyapunov Tracking Control via Backstepping

The TSE(3)-based UKF was implemented in [8, 37, 38] using the Morse-Lyapunov (M-L) controller from [6] and expanded to tracking control in [9]. The controller is defined as

$$u_0 = -\mathbb{I}^{-1} \left(\operatorname{ad}_{\hat{g}}^* \mathbb{I} \hat{\mathbb{V}} - \operatorname{Ad}_{\epsilon_g} \operatorname{ad}_{g_d}^* \mathbb{I} \mathbb{V}_d \right) - \epsilon_\tau + \operatorname{ad}_{\epsilon_\mathbb{V}} \operatorname{Ad}_{\epsilon_g} \mathbb{V}_d - \mathbb{I} K_1 \dot{l} - \mathbb{I} K_2 \psi - \mathbb{I} \kappa [0_{1 \times 3}^T \left(\epsilon_R \epsilon_r \right)^T]^T \in \mathbb{R}^6$$

where

$$\epsilon_{\tau} = \mathbb{I}^{-1}\hat{\tau} - \operatorname{Ad}_{\epsilon_{o}} \mathbb{I}^{-1} \tau_{d} \tag{23}$$

is the relative external forces and torques between the estimated and desired models, with an adjoint operator used to express the error in the approriate frame as discussed below Eq. (14) The gains $K_1 = \text{blkdiag}(k_{11}I_3, k_{12}I_3) \in \mathbb{R}^6 \ge 0$ and $K_2 = \text{blkdiag}(k_{21}I_3, k_{22}I_3) \in \mathbb{R}^{6\times 6} \ge 0$ are positive definite diagonal gain matrices and κ is a scalar gain coefficient. The backstepping function is defined as

$$\psi = \epsilon_{\mathbb{V}} + K_1 l(\epsilon_{\varrho}) \tag{24}$$

where

$$l(\epsilon_g) = [s^T(\epsilon_R), \epsilon_r^T]^T \tag{25}$$

such that

$$s(\epsilon_R) = \sum_{i=1}^3 a_i \left(\epsilon_R^T \hat{e}_i \right)^{\times} \hat{e}_i$$
 (26)

and $a \in \mathbb{R}^3$ is a vector of tunable gain values such that $1 \le a_1 < a_2 < a_3$ and \hat{e}_i (i = 1, 2, 3) are unit vectors aligned with the vehicle's principal axes. The time derivative of the Morse-Lyapunov function is shown to be negative for all (g, \mathbb{V}) except when $g = I_4$ and $\mathbb{V} = 0$, which is asymptotically stable equilibrium, and at saddle equilibria with unstable manifolds of zero-Lebesque measure, i.e. (diag(1, -1, -1, 1, 0), (diag(-1, -1, 1, 1, 0), and (diag(-1, 1, -1, 1, 0)) [6]. These critical points are isolated and thus have zero measure in TSE(3). Therefore, the equilibrium point $(g, \mathbb{V}) = (I, 0)$

is almost globally asymptotically stable. This work and the proof above are based on the Morse-Lyapunov controller fires introduced by [6] in which the positive definite Lyapunov function is augmented with a positive semidefinite Morse function in order to drive the backstepping function, ψ , and its derivatives to zero. The initial control force $u_0 \in \mathbb{R}^6$ is generated based on the desired control input from the M-L controller, and then constrained based on the spacecraft configuration. The control loop follows a structured sequence of estimation, optimization, and constraint enforcement. First, the control command is estimated based on the current state, then distributed optimally across constrained thrusters. Saturation limits and duty cycles are enforced before updating the estimated state. This approach is described in Algorithm 1. The numerical stability of this method has been demonstrated here and in previous work [14, 38], but further work is needed to prove the analytical stability of the controller and UKF.

As mentioned in Section II, standard optimization-based control methods struggle with constrained thruster configurations due to their reliance on continuous inputs, assumptions of convex constraints, and computational complexity. This method seeks only to optimize the distribution of thruster rather than its application. It takes what is fundamentally a very complicated optimization problem, i.e. how to get from pose and velocity "A" to pose and velocity "B" while minimizing fuel using some set of thrusters and mass properties and considering saturation limits, and simplifies it to a incremental operation where only the distribution of thrust is optimized. This means that the engineer must do more work offline, specifically controller gain tuning, UKF sigma point weight tuning, and deadband tuning. However, the end product is an algorithm that is intended to be computationally efficient enough to be run on the current generation of spacecraft while at the same time considering realistic challenges that an autonomous spacecraft is intended to face. Thus, by starting with a control input u_0 , the next step is to consider the optimal distribution of that control given some arbitrary configuration constraints.

While the Morse-Lyapunov controller generates a control command in the body frame of the vehicle, thruster constraints require additional steps to distribute control inputs across available actuators while respecting duty cycle and saturation limitations. Using the Adjoint operations for different reference frames discussed in Section III.B, the contribution of each individual thrusters may be considered. By adding these contributions up, a method of controlling a spacecraft of arbitrary thruster configurations may be devised.

V. Distributed, Constrained Control with Saturation Limits in the Presence of Uncertainty

In this section, several values of u are used. These values represent the control force as it goes through various transformations. The rationale for this will become clear in the following text, and a list of each superscript and subscript is provided in Section I. In short, u_0 is the initial control force calculated by the 6-DoF controller, in this case the M-L controller described in Section IV.B. u^* is the control force optimized to fit the constrained thruster configuration, assuming that the thruster configuration has access to the positive and negative components of all six degrees of freedom. u_d is the desired control force after imposing saturation limits on the optimized control force. u is the true control

force executed by the spacecraft after considering thruster noise, and \hat{u} is the estimated (or measured) control force based on residual analysis, used for fault detection, isolation, detection, and remediation. This notation is also used for c, c_0, u^*, c_d , and \hat{c} , for the ontime for each thruster correlating to each of u of the same notation.

Algorithm 1 Estimation and Control Sequence

```
Initializing:
```

Define Initial Conditions g_0 , V_0 , P_0

Begin Main Iteration Loop:

for k = 1, 2, ... do

- 1: Generate Ideal Control
 - $u_0 = u(\hat{g}_{k|k}, \hat{\mathbb{V}}_{k|k})$
- 2: Optimally Distribute Control Based on Spacecraft Configuration

$$\mathcal{J} = \min \left((\tilde{U}c^{\star} - u_0)^T (\tilde{U}c^{\star} - u_0) + D_1(\epsilon_g)c^{\star,T}c^{\star} + D_2 \sum_{n=1}^N \operatorname{ceil}(c_i^{\star}) \right)$$

$$u^{\star} = \tilde{U}c^{\star}$$

3: Impose duty cycle by scaling c^{\star} and recalculate control vector

$$c_{dc} = \frac{c^{\star}}{\max(c^{\star})} d_c$$

- $u_d = \tilde{U}c_{dc}$
- 4: For simulations, apply noise or anomalies to obtain true control vector $u = \tilde{U}c(1 + \mathcal{N}(0, \eta_T))$
- 5: Predict Based on Model Using UKF

$$[\hat{g}_{k+1|k}, \hat{\mathbb{V}}_{k+1|k}, P_{k+1|k}] \leftarrow [\hat{g}_{k|k}, \hat{\mathbb{V}}_{k|k}, P_{k|k}, u_d, \chi]$$

6: Propagate True State

$$[g_{k+1}, \mathbb{V}_{k+1}] = f(g_k, \mathbb{V}_k, u_k)$$

7: Obtain Expected and True Measurements

$$\hat{y} = h(\hat{g}_{k+1|k}, \hat{\nabla}_{k+1|k}, P_{k+1|k})$$

$$y = h(\hat{g}_{k+1}, \hat{\nabla}_{k+1}, \eta)$$

8: Update Based on Measurements

$$[\hat{g}_{k+1|k+1}, \hat{\mathbb{V}}_{k+1|k+1}, P_{k+1|k+1}] \leftarrow [\hat{g}_{k+1|k}, \hat{\mathbb{V}}_{k+1|k}, P_{k+1|k}, y, \hat{y}, \chi]$$

9: Update Variables

$$g_{k+1} = g_k, \, \mathbb{V}_{k+1} = \mathbb{V}_k, \, \hat{g}_{k|k} = g_{k+1|k+1}, \, \hat{\mathbb{V}}_{k|k} = \hat{\mathbb{V}}_{k+1|k+1}, \, P_{k|k} = P_{k+1|k+1}$$

end

A. Thruster Configuration Definitions for Autonomous Distributed Control

A distributed control scheme within the SE(3) framework requires an arbitrary control input while ensuring that the thruster configuration provides sufficient actuation authority across all six degrees of freedom. It is desired to determine how this control input is distributed about various actuators and how it determines the gimbaling of those actuators. To distribute control among arbitrary configurations thrusters, the components of such a control scheme must first be considered. A static thruster does not move, but when located away from the center of mass has contributions in both translational and rotational motion. The total translational and rotational control of the central body is assessed by assembling a matrix of the control input vectors representing each thruster with coefficients describing the maximum thrust of each thruster $T_{M,n} = [0;0;0;0;0;-T_n]$, where T_n is the force of thruster n and n0 is the total number of thrusters. The method of distributing the control input to the thrusters as presented as a potential optimization problem

such that

$$u_d = \sum_{n=1}^{N} u_n c_n = \sum_{n=1}^{N} Ad_{g_{\mathcal{M},n}^{-1}}^T T_{\mathcal{M},n} c_n \in \mathbb{R}^6$$
 (27)

which could be written as $u_d = \tilde{U}c \in \mathbb{R}^6$ where $\tilde{U} = [u_1, u_2, \cdots, u_N] \in \mathbb{R}^{6 \times N}$ is the mapping between individual thrusters and the body frame and c is the duty cycle that best matches the optimal distributed control u. The optimal coefficients for each thruster determined by Eq. (27) is obtained by solving the optimization problem of the form

$$\mathcal{J} = \min \left((\tilde{U}c^{\star} - u_0)^T (\tilde{U}c^{\star} - u_0) + D_1(\epsilon_g)c^{\star T}c^{\star} + D_2 \sum_{n=1}^N \operatorname{ceil}(c_n^{\star}) \right)$$

$$u^{\star} = \tilde{U}c^{\star}$$
(28)

This optimization problem is solved in this work using MATLAB's fmincon function to obtain c^* while imposing only that any index $c_i^* \ge 0$. The optimal value of c^* is determined such that $D_1, D_2 \in \mathbb{R}$ serve as scalar gains for the tuning of the deadband region. The gain $D_1(\epsilon_g)$ decreases as the spacecraft approaches its final desired pose, ensuring both adaptability and a bounded maximum magnitude. The gain D_2 remains static and is tuned to minimize propellant usage. The term $D_1(\epsilon_g)c^{*T}c^*$ establishes a 6-dimensional buffer zone around the pose to mitigate chattering, while $D_2\sum_{n=1}^N \operatorname{ceil}(c_i^*)$ prevents excessive thruster firings that could lead to actuator saturation or stuck thrusters. To enforce the necessary duty cycle ratios for a given maneuver, the optimization framework is extended into the time domain, incorporating predefined constraints on thruster duty cycles. Since certain spacecraft configurations may be suboptimal, residual motions along certain axes must be managed with appropriate thresholds to prevent controller saturation.

B. Robustness to Arbitrary Mass Properties

Consider the dynamics expressed in Eq. (10b) with the addition of some desired control input $u \in \mathbb{R}^6$. Alternatively, the control vector can be expressed as a distributed control scheme desribed in Equations (27) and (34). By separating the geometric frame from the body frame, Eq. (34) can be expressed as the product of two adjoints, i.e.

$$u_{0} = \sum_{i=1}^{N} \operatorname{Ad}_{g_{\mathcal{M}/\mathcal{B}}^{-1}}^{T} u_{i} c_{0,i} = \operatorname{Ad}_{g_{\mathcal{G}/\mathcal{B}}^{-1}}^{T} \sum_{i=1}^{N} \operatorname{Ad}_{g_{\mathcal{M}/\mathcal{G}}^{-1}}^{T} u_{i} c_{0,i} = \operatorname{Ad}_{g_{\mathcal{G}/\mathcal{B}}^{-1}}^{T} \tilde{U} c_{0}$$

$$(29)$$

Substituting the right hand side of Eq. (29) as u in Eq. (10b) yeilds

$$\dot{\epsilon}_{\mathbb{V}} = \dot{\mathbb{V}} - \operatorname{ad}_{\epsilon_{\mathbb{V}}} \operatorname{Ad}_{\epsilon_{g}} \mathbb{V}_{d} - \operatorname{Ad}_{\epsilon_{g}} \dot{\mathbb{V}}_{d} + \operatorname{Ad}_{g_{g/\mathcal{B}}^{-1}}^{T} \tilde{U} c_{0} \in \mathbb{R}^{6}$$

$$(30)$$

All of the mass terms (\mathbb{I} , $\mathrm{Ad}_{g_{G/\mathcal{B}}^{-1}}^T$) are then moved to one side, yielding

$$\operatorname{Ad}_{g_{G/B}^{-1}}\left(\mathbb{I}\epsilon_{\dot{\mathbb{V}}} - \operatorname{ad}_{\epsilon_{\mathbb{V}}}^{*}\mathbb{I}\epsilon_{\mathbb{V}} - \epsilon_{\tau}\right) = \tilde{U}c_{0} \tag{31}$$

A substitution for $\epsilon_{\hat{V}}$ is then performed using a version of Eq. (10b) with an arbitrary control input $u = u_0$, which results in

$$Ad_{g_{G/B}}u_0 = \tilde{U}c_0 \tag{32}$$

This equation indicates that there exists a coefficient $c_0 \in \mathbb{R}^N$ that maps the distributed control matrix $\tilde{U} \in \mathbb{R}^{6 \times N}$ to the desired control $u_0 \in \mathbb{R}^6$. However, constraints are imposed on either \tilde{U} or c_0 based on the spacecraft configuration. For instance, if no restrictions are placed on the coefficient vector c_0 , \tilde{U} must be full-rank to ensure complete controllability of the spacecraft across all six degrees of freedom. Furthermore, if the constraint $c_0 \geq 0$ is enforced, then \tilde{U} must not only be full rank but also contain both positive and negative values across all axes to maintain bidirectional actuation capability.

C. Saturation Limits

Several approaches for imposing saturation limits were evaluated during the development of this algorithm. It is found that imposing saturation limits on the control vector prior to distributing thrust was ineffective. Furthermore, imposing saturation limits within the optimization algorithm itself leads to unintended behavior, often resulting in all thrusters being active simultaneously. Instead, an effective approach is normalizing the vector of thruster on-time coefficients, c, which demonstrated stable and predictable behavior. This normalization be expressed as

$$c_{dc} = \frac{c^*}{\max(c^*)} d_c \tag{33}$$

where d_c is the maximum duty cycle within a given time step. For example, if a thruster can remain active for the entire duration of a one-second thruster firing period during a one-second time step, then $d_c = 1$. Conversely, if a thruster operates at 2 Hz with a full duty cycle of 0.1 second per duty cycle during a one-second time step, then $d_c = 0.2$. Using this information, the total control force applied to a spacecraft configuration with N thrusters is given by

$$u_d = \tilde{U}c_{dc} = \sum_{n=1}^{N} Ad_{g_{\mathcal{M},n}^{-1}}^{T} T_{\mathcal{M},n} c_{dc,n}$$
(34)

where \hat{u} is the estimated control forces commanded to the thrusters and c_{dc} is c^* adjusted to satisfy the imposed saturation limits. The value of c_{dc} is obtained as the best-fit solution within the constraints outlined in Eq. (28).

D. Anomaly Simulation and Detection

The anomaly considered in this work is a stuck thruster. The thruster firing history for any given timestep described above is augmented to simulate a continuously firing thruster. If thruster noise $\eta_T \sim \mathcal{N}(0, \xi)$ is included where \mathcal{N} is the normal Gaussian distribution with covariance ξ , this results in an estimated and true thruster firing history described by

$$u = \tilde{U}(c + \eta_T) \tag{35a}$$

$$\hat{u} = \mathbb{I}\hat{\mathbb{V}} - \mathrm{ad}_{\hat{\mathbb{V}}}^* \mathbb{I}\hat{\mathbb{V}} - \hat{\tau} \tag{35b}$$

where c is the true thruster firing pattern, u is true control, $\eta_T \in \mathbb{R}^N$ is the noise vector, and \hat{u} is the measured control. These are rearranged to give an expression for ontime error as

$$\epsilon_C = \tilde{U}^+(u_d - \hat{u}) \tag{36}$$

where $(\cdot)^+$ denotes the Moore-Penrose inverse, also known as the pseudo inverse. An error tolerance is established such that ϵ_c should not exceed the 3σ variance due to thruster noise. Any error beyond this threshold indicates off-nominal performance and will triggers the abort scenario. Since the true control force u is not directly observable, it must be estimated. By examining the residuals after taking the difference of the estimated control u_d and the measured control \hat{u}_d , an anomaly can be detected. Since the control force is not measured directly, the estimated states from the previous time step obtained using Eq. (5b) are used for anomaly detection.

E. Sensor Models

The sensor model in this work accounts for various sources of noise and bias sources a multiple sensor types, including gyroscopes, star trackers, and LIDAR. Uncertainty in box and sensor angles arise from ambiguities in the physical mounting position and orientation of the sensor on the spacecraft, as illustrated in Fig. 4. Bias can be due to manufacturing defects or inherent hardware imperfections. In some sensors, such as star trackers, bias may be static, often caused by a rounding errors in the orientation of the stars in the database relative to the true values. In contrast, in gyroscopes and accelerometers, biases are dynamic, originating in integration errors and random walk effects, each of which must be modeled and quantified separately. Noise is primarily characterized as non-integrated Gaussian noise, as commonly used in simulations, but is explicitly defined based on a specific value or parameter. In this work, sensors are modeled with box errors, sensor biases, and Gaussian noise properties of varying magnitudes listed in Table 1. Time-varying ambiguities, such as random walk and integration errors, are the subject of future study.

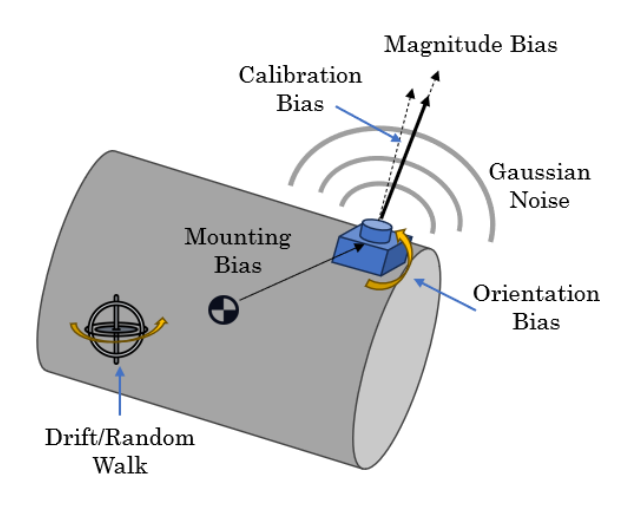


Fig. 4 Sources of sensor ambiguity

VI. Numerical Simulation & Modeling

Two case studies were considered in this work: a dynamic Gateway subject to plume forces from a simulated, large visiting vehicle attempting to dock. The second case study flips the perspective to consider a visiting vehicle performing an autonomous docking to a stationary Gateway, with tight constraints on successful docking criteria in attitude, position, angular rate, and translational velocity. It may have become evident that these are two parts of the same, complete problem. Because of the complexity of each and their role in the development of this algorithm, there were considered separately. In Section VII, the challenges of implementing a complete simulation are discussed.

In the first case study, three mass and thruster layouts were selected based on possible Gateway configurations for early Artemis missions. All configurations included the power and propulsion element (PPE) and the habitation and logistics outpost (HALO). Gateway Configuration 1 has no logistics module (LM). Gateway Configuration 2 has the LM docked axially to HALO. Gateway Configuration 3 has the LM docked radially to HALO and all are shown in Figure 5.

The distribution and magnitude of mass for each vehicle was randomized. This was done by making multiple slices along the length of the vehicle and then dividing those slices into four equal parts. Each *i*th part of the vehicle has a nominal mass m_i perturbed by \tilde{m}_i where $\tilde{m}_i \sim U(-0.75m_i, 0.75m_i)$. In Figure 5 the parts are scaled for the sake of visualization based on the mass dispersion. For this study, three slices are made resulting in 12 equal parts for each vehicle. Note that the solar arrays were not dispersed for this study. The PPE is assumed to be a rectangular prism while the HALO and LM vehicles are treated as hollow cylinders. With the mass dispersed, the center of gravity (CG) and moments of inertia can be determined first for each vehicle, then for the entire Gateway.

To further challenge the algorithm the thrusters are placed randomly along the surface of the PPE and LM. For simplicity, the thrusters are clustered into sets of three called triads. The thrusters within a triad are spaced evenly 120° apart radially and then canted up 20° towards the spin axis. The PPE and LM each have four triads dispersed over the surface. For the PPE, the dispersion for the jth triad is done by first randomly selecting one of the sides other than the

Table 1 Assumed Gateway and Scenario Properties.

PPE Properties					
Thruster [N]	F = 400				
Number of Thrusters [counts]	N = 12				
Specific Impulse [s]	$I_{sp} = 300$				
Dimensions [m]	w = 4, h = 4, l = 8				
Center of Mass [m]	$r_{cm} = [4, 0, 0]^T$				
Mass [kg]	$m_{\rm PPE} = 8000$				
Inertia [kg m ²]	J = diag([21333, 53333, 53333])				
PPE Solar Array Properties					
Dimensions [m]	w = 5, h = 0.05, l = 12				
Center of Mass [m]	$r_{cm} = [6, 0, 0]^T$				
Mass [kg]	$m_{\rm SA1} = 250$				
Inertia [kg m ²]	J = diag([521, 3130, 3521])				
HALO Properties					
Dimensions [m]	r = 2.2, l = 10				
Center of Mass [m]	$r_{cm} = [5, 0Ss, 0]^T$				
Mass [kg]	$m_{\rm HALO} = 12000$				
Inertia [kg m ²]	J = diag([42540, 121270, 121270])				
Idealized Reference Spacecraft					
Thruster [N]	F = 125				
Number of Thrusters [counts]	N = 8				
Specific Impulse [s]	$I_{sp} = 300$				
Dimensions [m]	$r = 2.2, \ l = 7$				
Center of Mass [m]	$r_{cm} = [0, 0, -0.25]^T$				
Mass [kg]	$m_{\rm SC} = 15000$				
Inertia [kg m ²]	J = diag([89750, 89750, 19050])				
	<u> </u>				

one docked with HALO. Then the location on the side is uniformly dispersed based on a percentage of the length, I_j , and width, w_j , of the side such that $I_j \sim U(0,1)$ and $w_j \sim U(0,1)$. Once placed on a location, the triad is rotated by the angle ζ_j such that $\zeta_j \sim U(0^\circ, 120^\circ)$. In the event that at least one thruster was not pointed in each direction, the thrusters are simply randomized again. A bias has been added to offset the otherwise Gaussian distribution of the mass properties. The center of mass of each element and total center of masses of each component as well as the total center of mass are displayed by alternating black and white spheres.

For the LM, the triads are only placed along the curved surface of the cylinder. The location on the cylinder is determined by randomly selecting a position along the length of the cylinder I_j and clock angle ϕ_j , relative to the center axis such that $I_j \sim U(0, I_{LM})$ and $\phi_j \sim U(0^\circ, 360^\circ)$ where I_{LM} is the total length of the LM defined in Table 1. Again, the triad is rotated by the angle ζ_j such that $\zeta_j \sim U(0^\circ, 120^\circ)$. The same check of thruster compatibility is done for the LM triads and is regenerated if necessary. Because the focus of this study is the algorithm, the effects

of self-impingement of the thruster plumes are ignored. The goal is to prove the robustness of the algorithm and not necessarily solve the complicated control problem of Gateway.

As mentioned above, three Gateway configurations illustrated in Fig. 5 are built and considered against an idealized, fully controllable, 8-thruster reference spacecraft configuration with an ideal center of mass located very close to its geometric center. All vehicles were exposed to a pluming force of $\tau = [L_p^T, f_p^T]^T$ over the course of 60 seconds, where $L_p = [50e^{-t}, 3e^{-t}, 10e^{-t}]^T$ and $f = [e^{-t/2}, 120e^{-t/2}, 0.1e^{-t/2}]^T$. This force is generated in order to estimate pluming induced by a large incoming visiting vehicle or human landing system, which induces both torques and forces on the Gateway. This force is the same across all configurations and the LM reference model. All vehicles are assumed to be located near apolune of the near-rectilinear halo orbit and external forces and torques due to solar radiation pressure, astronomical bodies, and gravity gradient torques are not considered, as they would be negligible during the integration time compared to these induced forces and torques. The physical properties of the vehicles and modules are described in Table 1.

The simulation was run no less than 30 times to test the resiliency of the algorithm. All 30 trials had randomized mass properties and thruster configurations within the boundaries described above. In all cases, very similar performance was observed with the final stability of Configuration 1 having the most variability from case to case, but in all trials was able maintain stable attitude with $< 1 \times 10^{-5}$ rad/s residual angular motion and < 0.4 m/s residual translational motion. Other cases had small residuals in translational motion at < 0.05 m/s. Gain tuning for this specific scenario can improve stability if thruster configurations are known, however this work demonstrates that even in the worst off-nominal

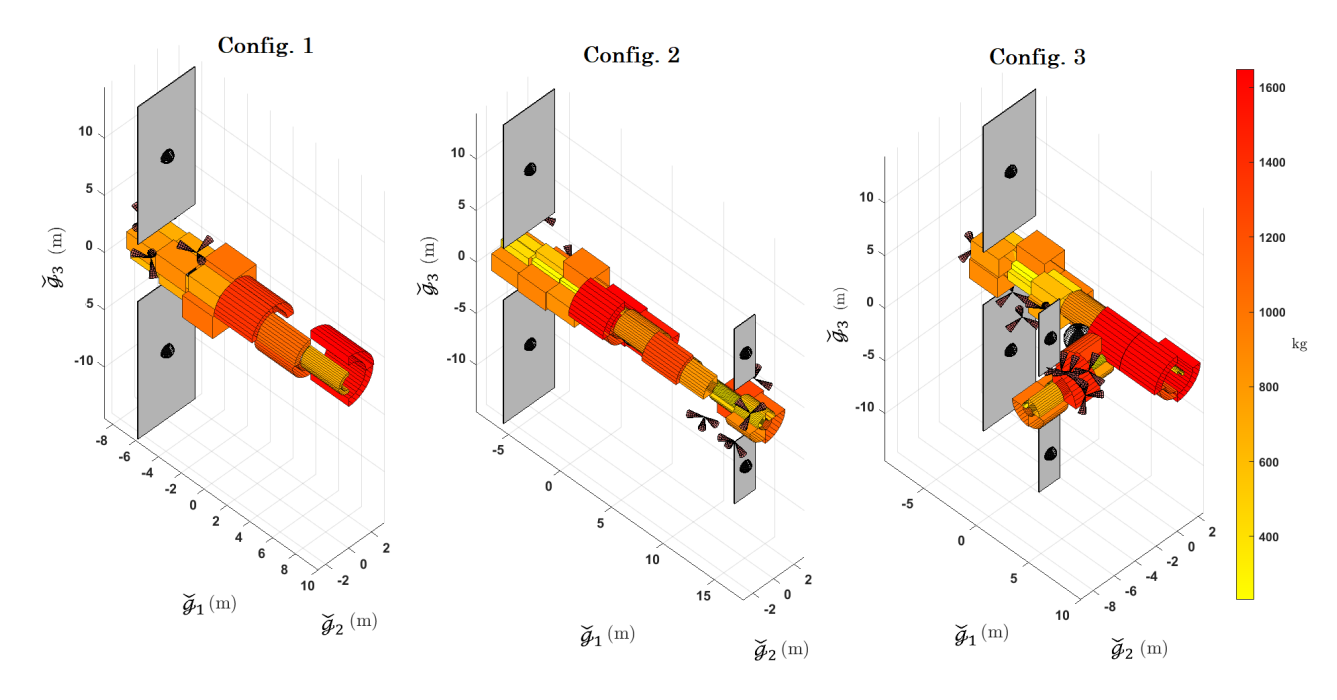


Fig. 5 Scenario 1: Gateway configurations with random thruster positions and mass properties for each module.

Table 2 Logistics Module Properties. Error values are 3σ distributions.

Value					
hicle					
F=400					
N = 12					
$I_{sp} = 300$					
r = 2.2, l = 7					
$r_{cm} = [3.5, 0, 0]^T$					
$m_{\rm LM} = 15000$					
J = diag([27013, 54340, 54340])					
w = 2, h = 0.05, l = 6					
$r_{cm} = [3, 0, 0]^T$					
$m_{\rm SA2} = 75$					
J = diag([25, 231, 250])					
yro					
$B_{r,G} = 0.01$					
$B_{\theta,G} = 0.1$					
$\eta_{\omega} = 0.0025$					
Tracker					
$B_{r,ST} = 0.01$					
$B_{\theta,ST} = 0.1$					
$\eta_{\theta} = 0.0025$					
Angle Noise $(\frac{o}{s})$ $\eta_{\theta} = 0.0025$ LIDAR					
$B_{r,LIDAR} = 0.01$					
$B_{\theta, LIDAR} = 0.1$					
$\eta_r = 1$					
$\eta_{v} = 0.01$					
Properties					
$B_p = 0.01$					
$B_{\theta,1}, B_{\theta,2} = 0.1$					
$\eta_T = 5$					

circumstance, catastrophic instability is avoided.

For the second case study, the mass properties of the LM are assumed to be known and the ambiguity is instead in the sensor and thruster magnitude, position, orientation. A table showing the magnitudes of these randomly selected values are listed in Table 2, as well as more precise values for the LM. The vehicle is modeled as a cylinder with a diameter of 4 m and a length of 8 m, with the difference between the \mathcal{G} and \mathcal{B}^1 modeled as a displacement long the center of mass equal to ${}^{\mathcal{B}^1}r_{\mathcal{G}}=[-4,0,0]^T$ m, with the origin of the \mathcal{G} frame centered about the docking adapter. The vehicle's thruster configuration consist of 8 delta-V thrusters aligned with but displaced from the g_1 axis of the vehicle, and 8 maneuvering thrusters in pairs separated by 90^o all with some $-\check{g}_1$ component, and 4 each with primarily $\pm\check{g}_2$ and

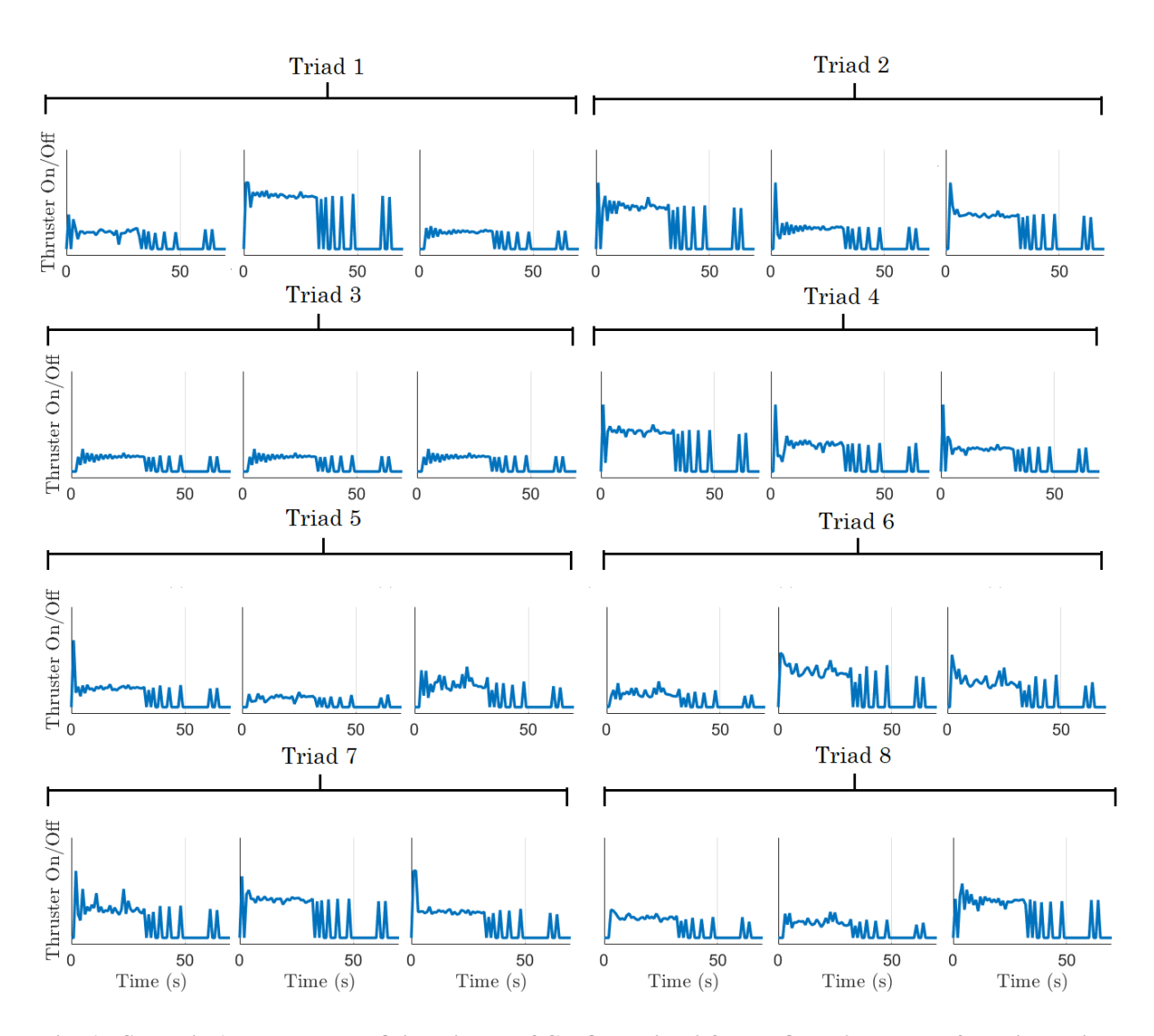


Fig. 6 Scenario 1: The thruster firing history of Configuration 2 for the first 70 seconds of the simulation.

 $\pm \check{g}_3$ components. Mass loss as a function of fuel use is not considered, as the largest estimates assume the depletion of approximately 1% of the vehicle's mass during the RPOD maneuver.

A. Scenario 1: Gateway Stationkeeping

The TSE(3)-UKF used in this work employs a dynamic model and a measurement model that estimates pose and augmented velocity. Thruster noise is also considered whenever the thrusters are fired, modeled as a noise parameter. The list of noise values used in this work is provided in Table 2 where (m) denotes measurement noise while (p) denotes process noise. The cutoff time of the pluming force can be seen as a black dashed line in Fig. 7. Solid lines denote the roll or x- axis, dashed lines denote the pitch or y- axis, and dotted lines denote the yaw or z- axis, depending on if the the attitude or position plot, respectively. The idealized spacecraft reference vehicle has a longer convergence time due

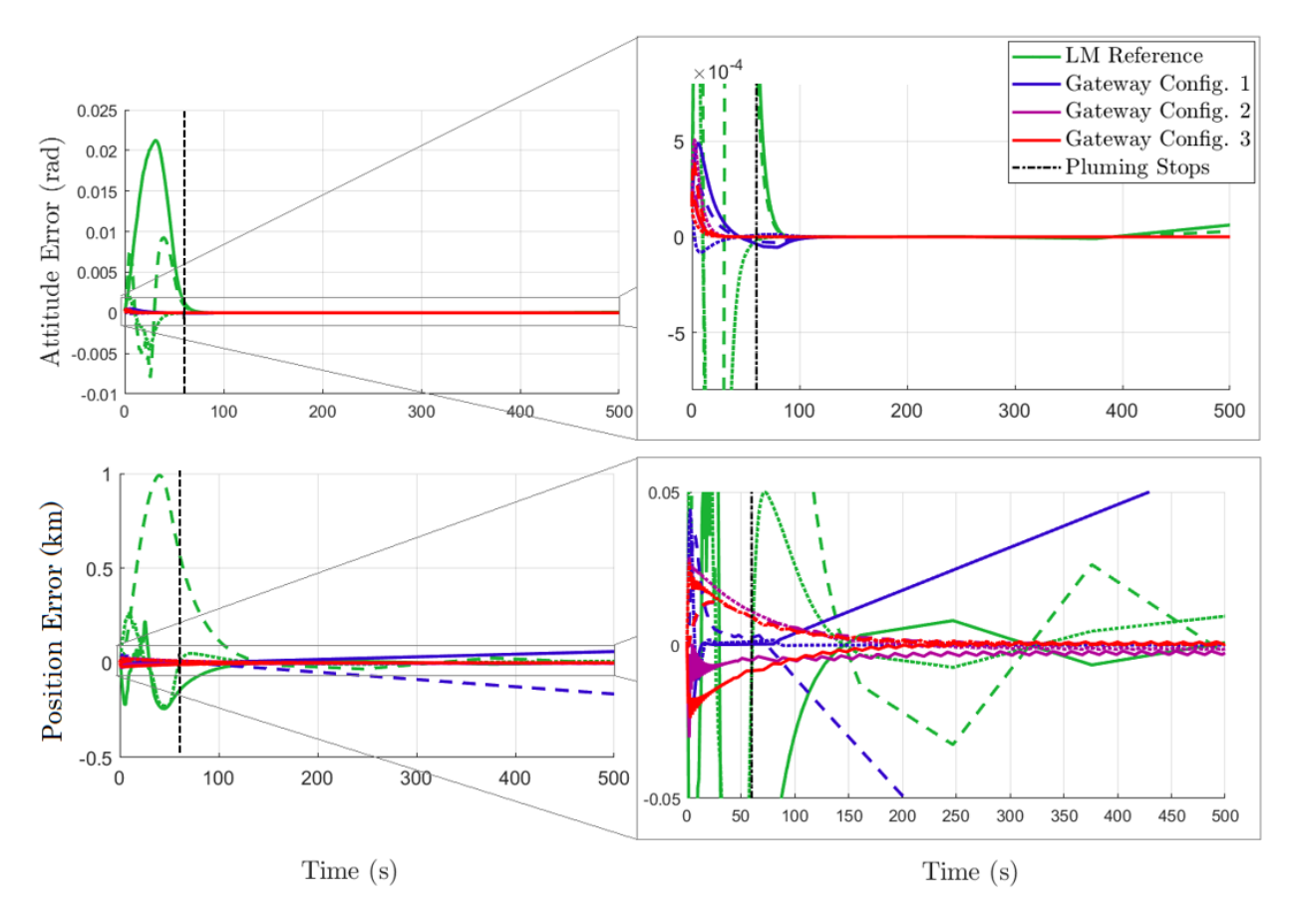


Fig. 7 Scenario 1: The translational and rotational motion of various configurations over time.

to its smaller mass and weaker thrusters. The dead band zone seen in the zoomed subfigures is likewise due to the significantly lower mass, causing maneuvers to be far more sensitive. The jitter in position and attitude, expressed as Euler angles in Figure 7, is due to the binary nature of the RCS thrusters modeled as they turn on and off in an effort to stabilize the system. The divergence of Gateway Configuration 1 is likely due to instability caused by all thrusters located at one end of the vehicle, but early results suggest that this could be overcome by fine-tuning gains for this specific configuration. Nevertheless, attitude convergence across all configurations and the logistics module is good,

Table 3 UKF Weights and Process Noise Properties

Parameter	Value	Parameter	Value
α_p	9	γ_p	1
α_q	18	γ_q	1
α_u	7.9	γ_u	1
eta_p	9	$\eta_{\theta,p}$ (rad)	$\frac{\pi}{360}$
eta_q	18	$\eta_{r,p}$ (m)	1
eta_u	7.9	$\eta_{\omega,p} \left(\frac{\mathrm{rad}}{\mathrm{s}} \right)$	$\frac{\pi}{3600}$
		$\eta_{v,p} \left(\frac{\mathrm{m}}{\mathrm{s}} \right)$	0.01

Table 4 Controller Gains

Scenario	k ₁₁	k ₁₂	k ₂₁	k ₂₂	К
1a	0.09	0.5	0.1	0.1	0.1
1b	0.09	0.015	0.5	1.9	0.01
1c	0.09	0.015	0.5	1.9	0.01
1d	0.09	0.015	0.3	0.5	0.01
2	0.095	0.0195	0.5	0.5	0.02

and the position for all vehicles remains within a couple of hundred meters over the course of the simulation, with most remaining within a few meters. Although only one demonstration of each randomized configuration is illustrated here, over 30 randomized placements of thruster positions and mass properties were tested with nearly identical performance each time, demonstrating that the method described herein is capable of performing regardless of what configuration it is provided. As seen in Fig. 7, most of the convergence occurs rapidly, with only small changes being made to overcome the exponentially decreasing plume force and to reorient and reposition the vehicle at the desired pose. The constraints of the randomly configured thruster mean that the vehicle cannot exactly perform the idealized M-L control, so some deviation occurs between the desired control and true control resulting in the zig-zag oscillations as the vehicle converges closer to the desired state as $t \to \infty$. Fig. 6 demonstrates the performance of the first 24 thrusters over the course of the simulation, with the normalized magnitude of each thruster during a designated duty cycle being indicated by the vertical axis. The oscillations in (Fig. 6) result directly from discrete duty cycle enforcement and deadband constraints, which limit continuous control actuation. While the system remains stable, future work could explore alternative filtering strategies to reduce control chattering.

B. Scenario 2: Autonomous RPOD

As an extension to [14] and [10], measurement and process noise interpreted with a UKF on SE(3) [24, 25] has been included. Furthermore, thruster noise has been added to the system, which introduces uncertainty in control output. Finally, the criteria for a successful soft capture (docking) have been significantly tightened, with a required docking attitude error of less than $\pm 1^{\circ}$, position error of less than ± 0.1 m, angular velocity error of less than 0.01° /s, and velocity of 7 ± 0.5 cm/s. The control of the spacecraft is accomplished using a tracking M-L controller described by [6, 9] and introduced in Section IV.B.

The approach profile for the RPOD simulation, illustrated in Fig. 9, consists of a reference trajectory created using a 3-DoF simulation with impulse burns to create each phase. The alternating purple and teal segments are different phases of the reference trajectory, while the green line is the true state, the dark blue is the estimated state, and the light blue are the measured states. The simulation begins with a one-minute initialization to simulate Gateway capturing the Logistics Module's signal at a distance of 10 km. This is followed by a roughly 17-minute approach at 4.7 m/s. As the LM nears

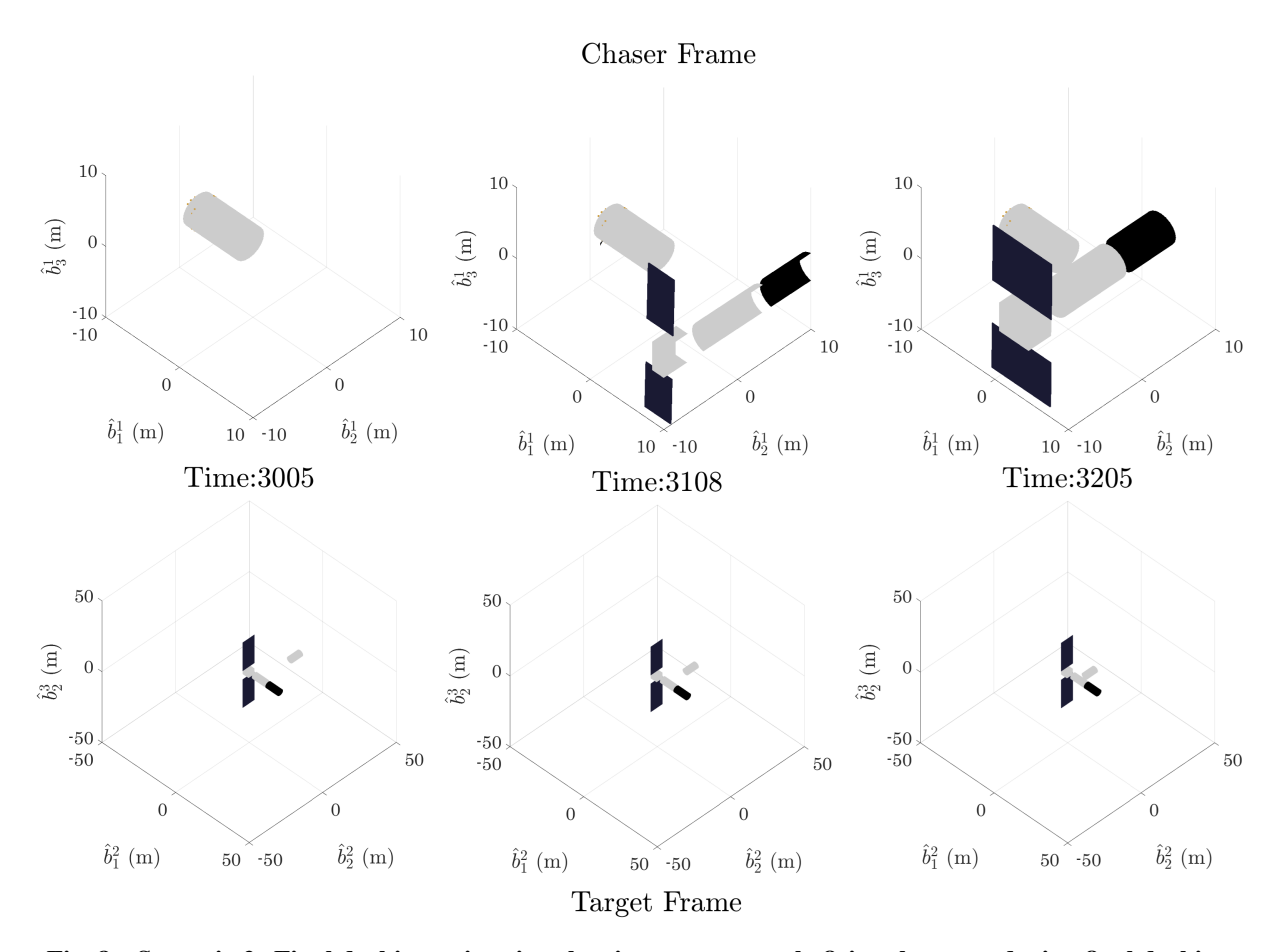


Fig. 8 Scenario 2: Final docking animation showing autonomously firing thrusters during final docking.

the 200 m area around Gateway known as the Keep-out-Sphere (KoS), it slows to 1.8 m/s for 10 minutes before holding outside of the KoS for 6 minutes to simulate awaiting permission to dock. The vehicle then begins a close approach aligned with the docking port at 30 cm/s for about 12 minutes, then a docking burn is performed to slow the vehicle to 7.7 cm/s for the final 9 minutes before capture. This 3-DoF simulation is then used as a reference from which to build the 6-DoF counterpart. The desired vehicle attitude is set to be facing along the (relative) negative velocity direction during approach to allow the delta-V thrusters more efficient braking. The delta-V thrusters are positioned at the rear of the vehicle facing along the $-\check{b}_1^1$ direction. During the hold at the edge of the KoS, the vehicle desired attitude of the spacecraft is one in which the first principal axis points along the Gateway \check{b}_2^2 (docking axis), and the \check{b}_3^1 and \check{b}_3^2 axes are desired to be aligned. Desired angular velocity for the trajectory is set to $\omega = 0_{3\times 1}$.

A deadband is imposed for the control that can be tuned to obtain the desired load on the jet firing history. With no deadband, thrusters constantly fire in an attempt to perfectly match the desired pose. By allowing the vehicle to drift freely when tighter constraints on pose are not needed, a more fuel-efficient approach is obtained. Since there has never been an RPOD operation for vehicles similar to what is simulated in this work, it is difficult to say with certainty to what benchmark these numbers can be compared. For similar operations with the International Space Station, a delta-V

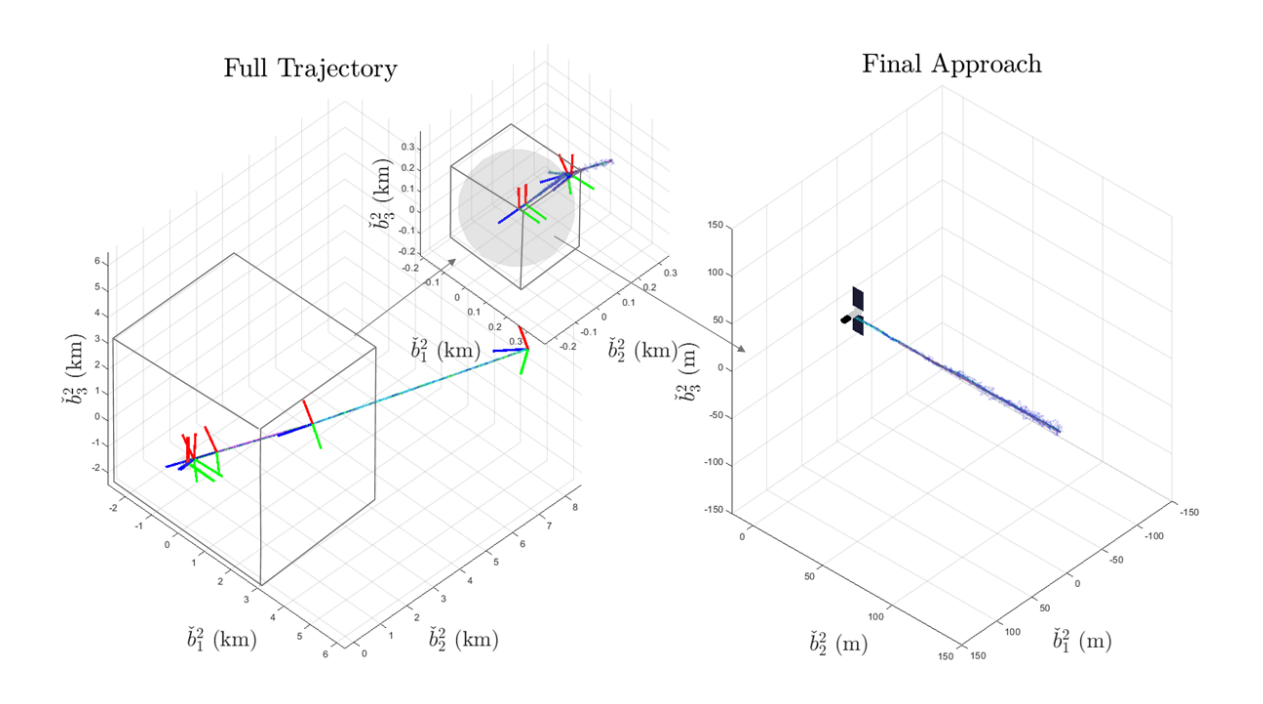


Fig. 9 Scenario 2: RPOD simulation of the LM using a 3-DoF reference trajectory with impulse burns.

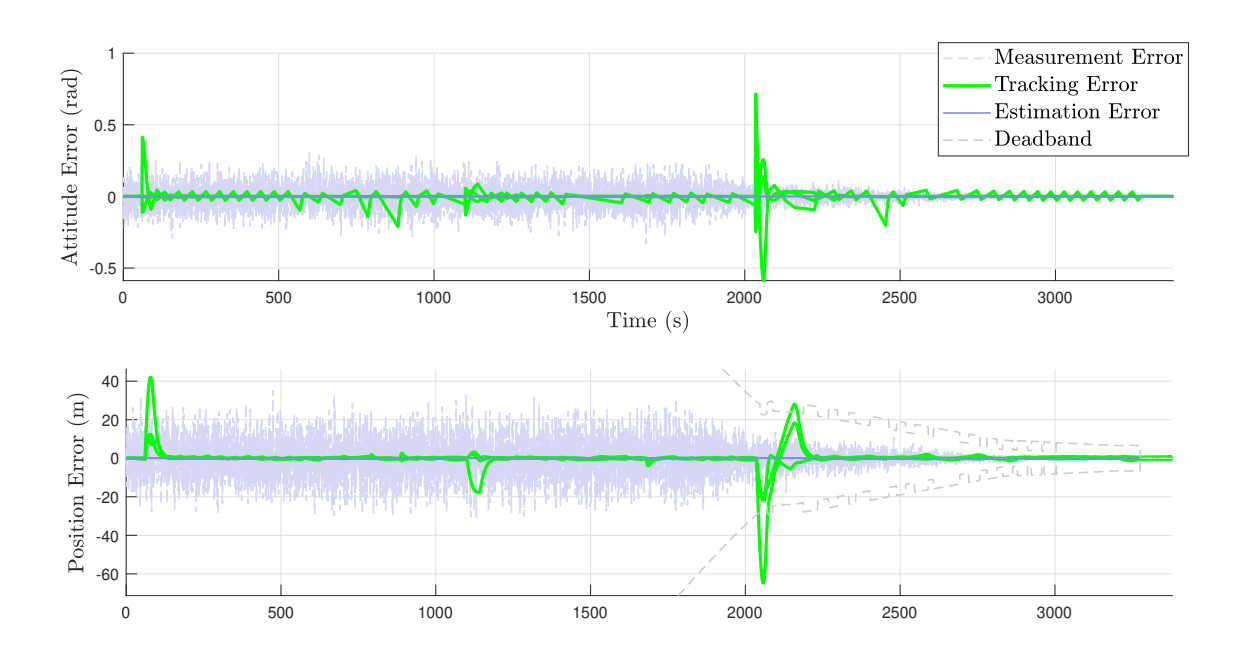


Fig. 10 Scenario 2: The position and attitude tracking and estimation error.

budget of around ~ 5 m/s is realistic. However, the vehicles that dock to the ISS have thruster configurations with more control authority in six degrees of freedom, tighter constraints on and greater knowledge off mass properties, and significantly more accurate measurement models. Furthermore, though not yet considered in this work, is the dynamic

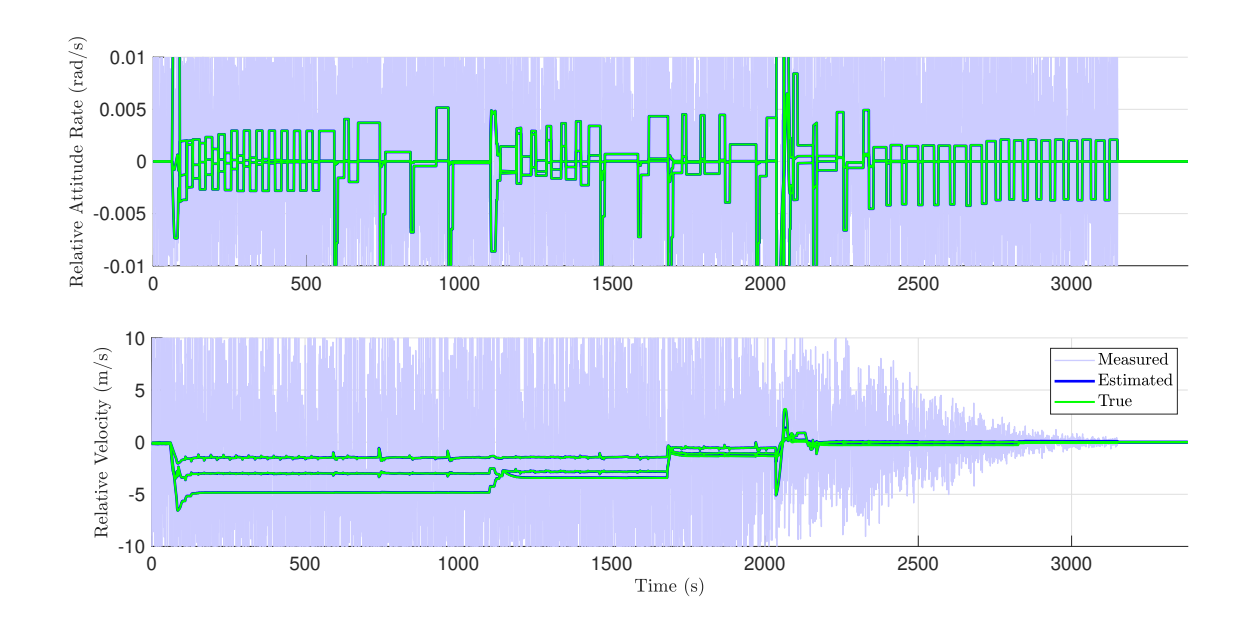


Fig. 11 Scenario 2: The angular rate and velocity tracking and estimation error.

motion of Gateway due to pluming effects. The propellant usage depicted in Figure 14 is expected to improve as this method is refined and great knowledge is gained about the dynamic environment in which the Gateway is expected to reside.

In thi work, the deadband constraints are set as $D_1(\epsilon_g) = 0.1 \|\epsilon_r\| + \|\epsilon_R\|$ and $D_2 = 100$. The relative position is visible in the tracking, measurement, and estimation errors illustrated in Fig. 10 and 11. Tracking error in attitude and position are more noticeable and a result of the spacecraft's inertia - something that is not modeled in the 3-DoF reference trajectory and thus inevitably causes discrepancies as the vehicle seeks to track instantaneous velocity changes. LIDAR signal acquisition is modeled when the vehicle meets relative attitude and position requirements, simulating the chaser having line-of-sight of Gateway's retro-reflectors at the radial docking port. After signal acquisition is achieved, position uncertainty is reduced and becomes a function of distance, shrinking linearly with distance until soft capture at the specified docking port. The jagged behavior in the top plot in Fig. 11 is the result of the deadband region, allowing the vehicle to oscillate gently between two states that are constrained by the duty cycle limitations of the thrusters. The authors wish to draw the reader's attention to the magnitude of this oscillation, which is around 0.005 rad/s in the presence of measurement uncertainty roughly an order of magnitude greater. The bottom plot of Fig. 11 also shows some jitter caused by the deadbanding, but this is not considered an issue especially considering the velocity error on the order of 5 m/s until LIDAR signal is acquired with Gateway, at which time the velocity uncertainty becomes a function of relative distance.

The control input from the M-L controller, the estimated distributed control, and the true distributed control are illustrated in Fig. 12. The attitude component of the M-L control is particularly affected by the saturation limits imposed

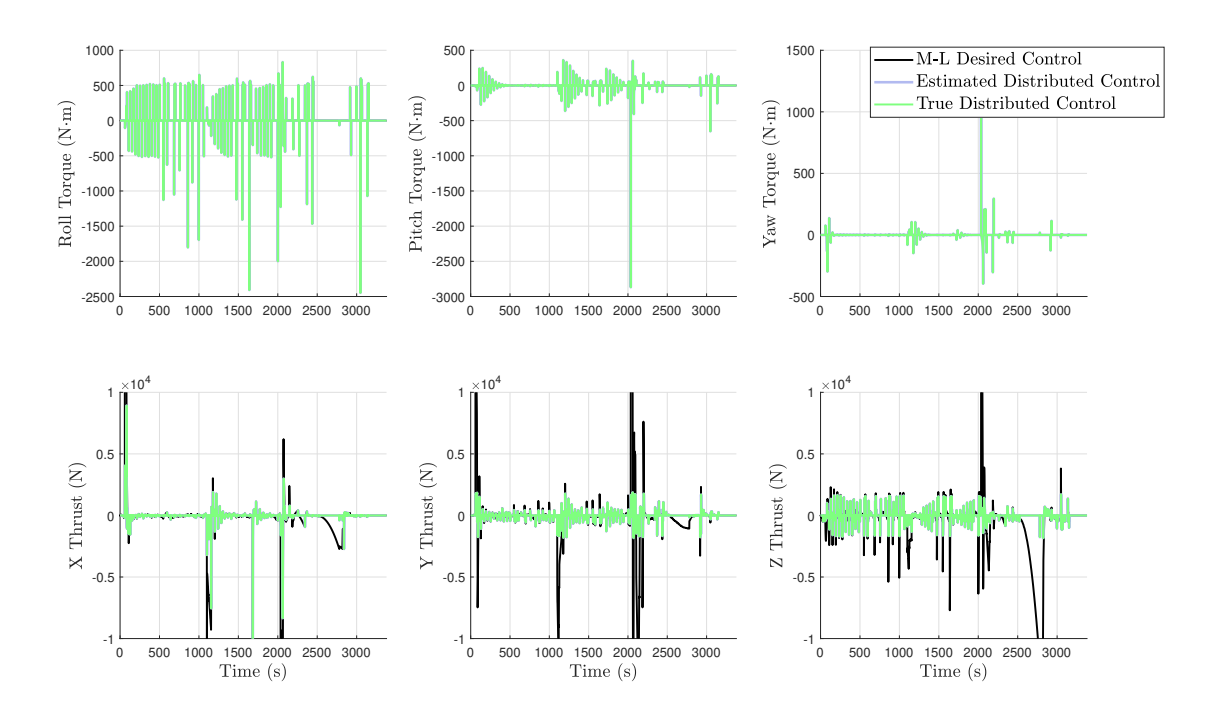


Fig. 12 Scenario 2: The desired M-L control compared to the estimated and true control input.

by the given thruster configuration, making it impossible to achieve the desired attitude rates while maintaining a controlled translational approach. However, the desired final pose is obtained by gradually pursuing the the optimal available jet firing histories over the simulation time. The oscillatory behavior of the true and estimated thruster input is a again result of the given thruster configuration in which all the thrusters are mounted in one end of the vehicle and the center of mass of the vehicle lies outside of the geometric center of the thrusters.

The jet firing history resulting from the control input in Fig. 12 is illustrated in Fig. 13, where the y-axis is scaled as on/off or, alternatively, as a normalized value between d_c and 0 when $d_c \neq 1$. These values are not distributed and constrained, but not discritized. Final values dock with an error in roll, pitch, and yaw less that 1 degree, a position error less than 6 cm, an attitude rate error of less than 0.1 deg/s, and at a velocity of 7.9 cm/s.

The top portion of Fig. 15 shows the the controller input as a function of gains k_{ij} and κ . Since these Gain values are static and driven by the nonlinear error between the desired and estimated state, it is more convenient to show the controller response to these gains and not the gains themselves, which are listed in Table 4. This plot is useful in offline gain tuning to optimize performance before launch. In this case, the plot shows that the most volatile component of this control approach is the k_{22} portion of the controller, which acts primarily (though not exclusively) on the error in the velocity component ϵ_{ν} . It is worth stating that during the tuning of the controller, the authors found that lowering the most volatile component of the this gain plot helped facilitate convergence and save time. Furthermore, the relationship between the given gain and the corresponding error usually suggested that the corresponding gain to the error was

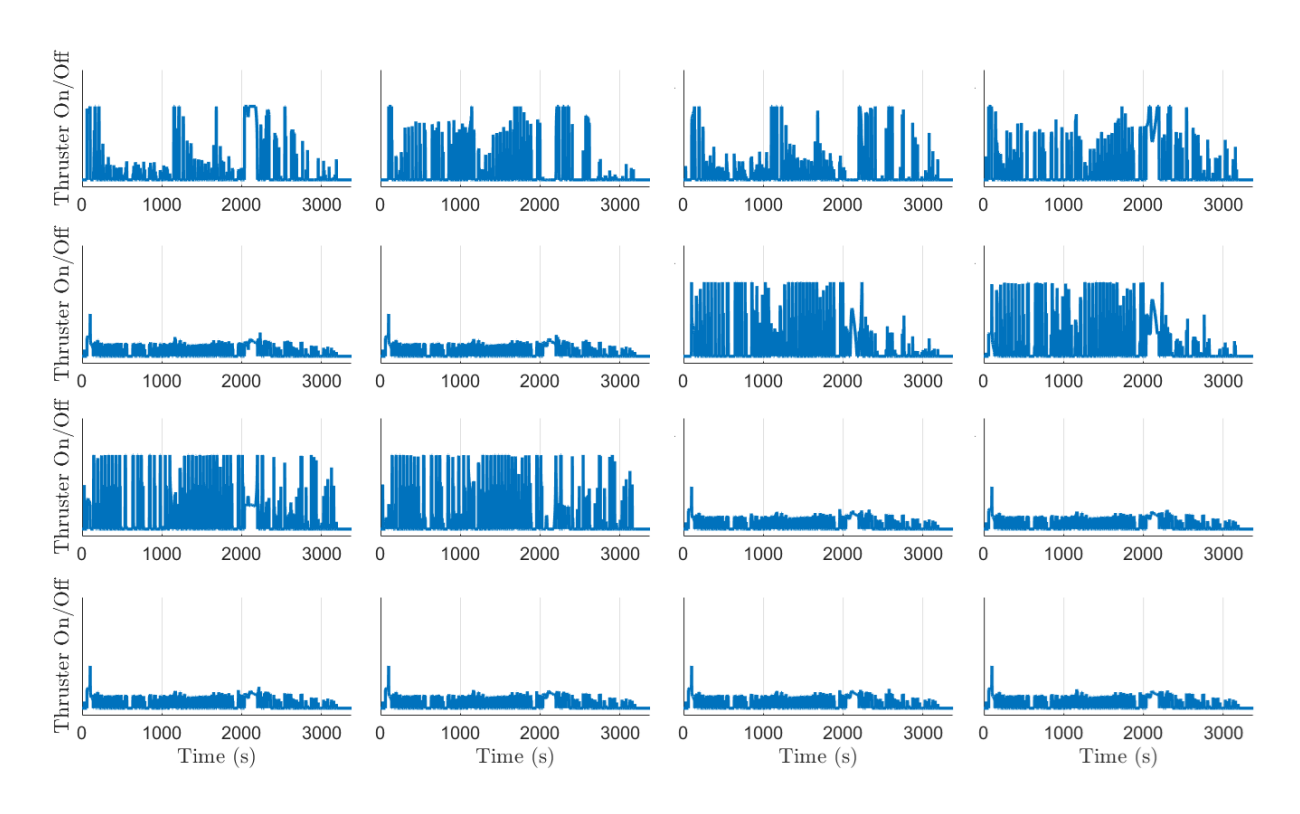


Fig. 13 Scenario 2: The distributed jet firing history during a nominal RPOD trajectory.

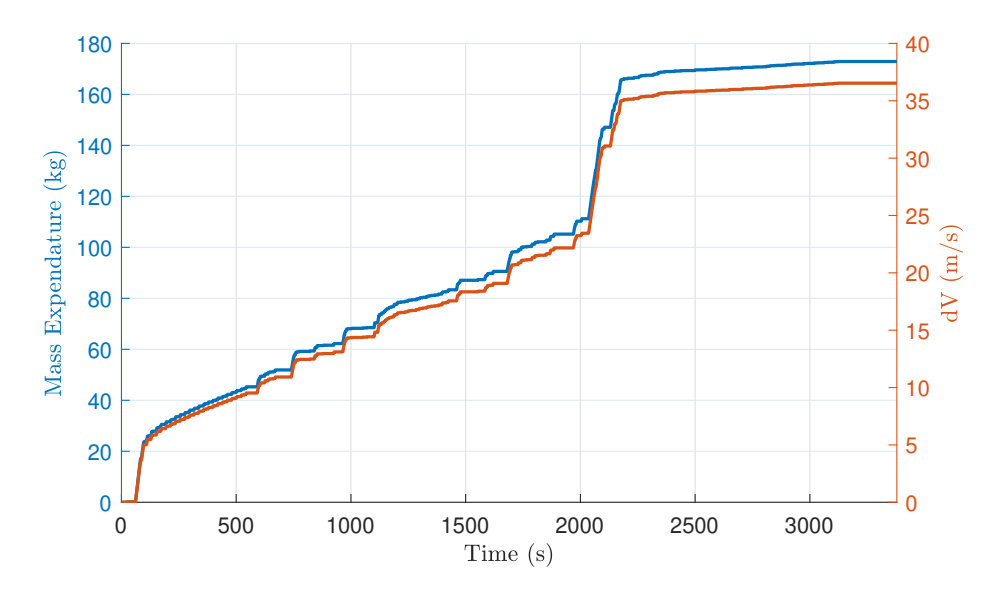


Fig. 14 Scenario 2: The propellant used for the full, nominal RPOD trajectory.

inadequate, in this case the k_{21} , which corresponds to the error in angular velocity ϵ_{ω} .

The propellant use during the nominal RPOD simulation, both in terms of delta-V and propellant mass, is illustrated in Fig. 14. The values of around 100 kg and 20 to 25 m/s align with expected values for a vehicle of this size and for these approach speeds. Other burns required for rendezvous between spacecraft such as the insertion burn into

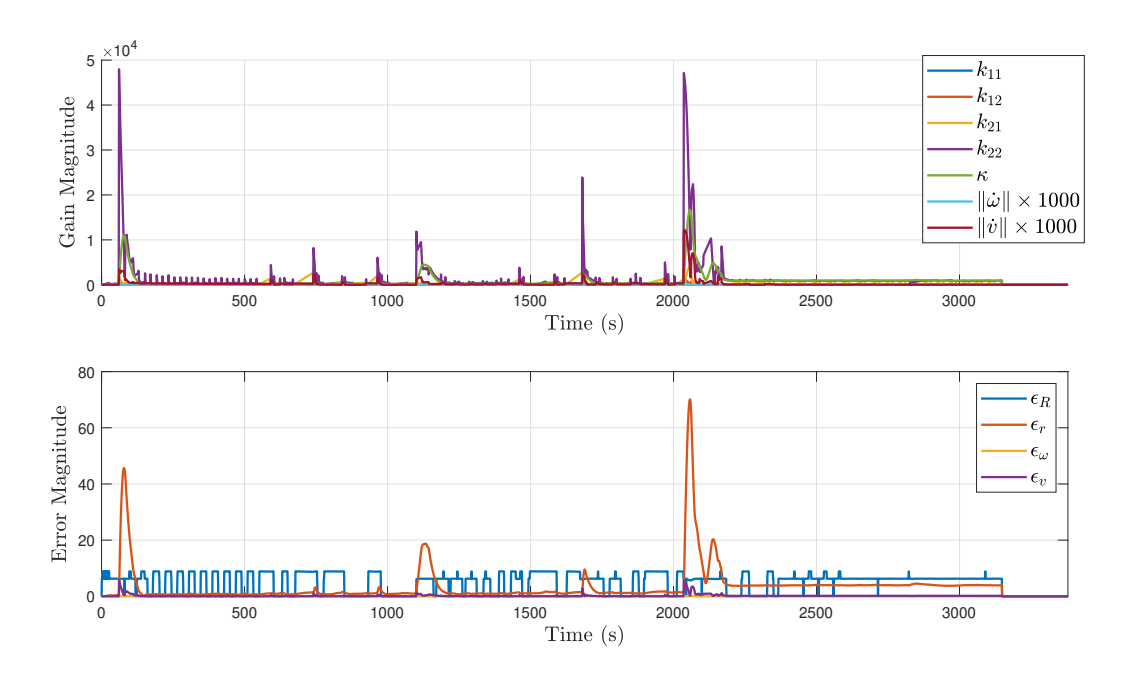


Fig. 15 Scenario 2: The gains and error magnitudes resulting from the distributed, constrained M-L control

the orbit are not considered. Fuel efficiency can be improved by allowing the vehicle to drift freely when strict pose constraints are unnecessary. Without a deadband, thrusters continuously fire in an attempt to precisely match the desired pose, leading to excessive fuel consumption. By introducing a deadband in the control logic, the system minimizes unnecessary thruster activations while still maintaining acceptable position and attitude constraints. The deadband constraint used in this work is defined as the terms with D_1 and D_2 coefficients in Eq. (28). The effects of this approach on relative position tracking, measurement, and estimation errors are illustrated in Figures 10 and 11.

VII. Conclusion

This work developed an autonomous thruster control framework that enables spacecraft with arbitrary configurations and arbitrary mass and thruster properties to maintain robust control. The approach integrates a TSE(3)-based unscented Kalman filter (UKF) with Morse-Lyapunov tracking, ensuring reliable station-keeping and rendezvous, proximity operations, and docking (RPOD) performance under high uncertainty. Such constraints include that the thruster configuration has access to both the positive and negative component of each of the six degrees of freedom. Duty cycle considerations for the reaction control system (RCS) with thruster noise is considered when guiding arbitrarily-configured spacecraft to a desired pose, even if that pose is not reachable in the presence of saturation limits within a single time step. The algorithm described herein relaxes many of the assumptions in previous work [10, 14, 29] and is demonstrated to perform well even when that configuration is not ideal in terms of controllability, i.e. thrusters and mass properties are randomly assembled and no consideration is made for ideal thruster placement or mass properties. This method

enables a spacecraft to meet its desired objective even when thrusters may have failed or when the configuration of the spacecraft has changed, both in terms of thruster configuration and mass properties. Furthermore, it is demonstrated that this method still works when sensor and process noise are included and filtered using the proposed UKF. When combined with other work in mass property estimation [8, 12, 15], these methods lay the theoretical framework for autonomous cargo management in space for vehicles with unknown mass properties. Two simulation results are provided. The first is for a scenario in which a Morse-Lyapunov-based controller [6, 8, 9, 38] that is implemented to obtain a closed-loop solution where RCS thruster placement and mass properties are randomly generated and placed about a roughly Gateway-shaped configuration. Thruster placement and mass properties are constrained to be realistic, but allowed to vary considerably. The second set of simulation results show that a complete RPOD scenario with strict success criteria placed on final attitude, position, angular rate, and velocity is achievable even in the presence of broad uncertainties.

Several challenges are associated with this implementation. First, a key concern is that a dynamically controlled Gateway, focused on stationkeeping, may introduce instability as the chaser attempts to track a moving docking port. Second, the simulation would require integrating computational fluid dynamics to model plume forces, a non-rigid body model to account for solar panel flexing, and two distinct control schemes operating at a common frequency. Due to the complexity of this effort, it is designated as the focus of a separate study, which will be submitted for publication in the near future. Future extensions may incorporate adaptive gain tuning and in-orbit validation to enhance real-time autonomy and robustness against actuator failures. Furthermore, improved filtering techniques could reduce residual control oscillations observed in simulation.

VIII. Acknowledgments

The authors would like to acknowledge Chuck Weyandt of Aegis Aerospace as part of NASA's Deep Space Logistics Project Office for providing valuable insight in spacecraft hardware bias and measurement errors.

IX. Relevant Funding Information

The lead author is employed by the National Aeronautics and Space Administration, which has funded the majority of this work. This work was also partially supported by NASA through Aegis Aerospace under contract No. 80KSC021F0014 and through a.i. Solutions under contract No. AIS-E3-22-005.

References

[1] Hashimoto, T., Kubota, T., Kawaguchi, J., Uo, M., Baba, K., and Yamashita, T., "Autonomous descent and touch-down via optical sensors," *Advances in the Astronautical Sciences*, Vol. 108 I, 2001, pp. 469–480. Proceedings of the AAS/AIAA Space Flight Mechanics Meeting; Conference date: 11-02-2001 Through 15-02-2001.

- [2] Pei, J., Choueiri, M. N., Elandt, R., Peck, M. A., and Finch, P., "An Innovative Control Allocation Scheme to Address Reaction Thruster Interactions on a 3U CubeSat," *AIAA Guidance, Navigation, and Control Conference*, 2018. https://doi.org/10.2514/6.2018-2096, URL https://arc.aiaa.org/doi/abs/10.2514/6.2018-2096.
- [3] Koditschek, D., "The Application of Total Energy as a Lyapunov Function for Mechanical Control Systems," *Contemporary Mathematics, American Mathematical Society*, Vol. 97, 1989. https://doi.org/10.1090/conm/097/1021035.
- [4] Chaturvedi, N., and McClamroch, N. H., "Almost global attitude stabilization of an orbiting satellite including gravity gradient and control saturation effects," 2006 American Control Conference, 2006, pp. 6 pp.—. https://doi.org/10.1109/ACC.2006.1656472.
- [5] Velichenko, V. V., "Geometric mechanics: Foundations of the theory and fundamental equations," *Journal of Applied Mathematics and Mechanics*, Vol. 78, No. 3, 2014, pp. 305–313. https://doi.org/10.1016/j.jappmathmech.2014.09.014.
- [6] Nazari, M., Butcher, E. A., and Sanyal, A. K., "Spacecraft attitude fractional feedback control using rotation matrices and exponential coordinates," *Journal of Guidance, Control, and Dynamics*, Vol. 41, No. 10, 2018, pp. 2185–2198. https://doi.org/10.2514/1.G002956.
- [7] Wang, J., Butcher, E. A., and Yucelen, T., "Consensus Estimation of Rigid Body Motion Using Lie Algebra se(3) and the Consensus Extended Kalman Filter," *AIAA SciTech 2019 Forum*, 2019. https://doi.org/10.2514/6.2019-1163.
- [8] McCann, B., V. Gunter, H., Nazari, M., and Henderson, T., "Generalized Formalism for Variable-Mass-Property Spacecraft Dynamics Utilizing Rigid Body Motion on Lie Groups," AIAA/AAS Astrodynamics Specialist Conference, Vol. 22-790, 2022.
- [9] Mangiacapra, G., Wittal, M., Capello, E., and Nazari, M., "Unscented Kalman filter and control on TSE(3) with application to spacecraft dynamics," *Nonlinear Dynamics*, Vol. 108, 2022, pp. 2127–2146. https://doi.org/10.1007/s11071-022-07293-x.
- [10] Wittal, M. M., Asher, B. W., and Nazari, M., "Autonomous RPOD for Arbitrarily Configured Spacecraft with Anomaly Detection," 2024 AAS Astrodynamcis Specialist Conference, 2024.
- [11] Nazari, M., Canales Garcia, D., McCann, B. S., Butcher, E. A., and Howell, K., "Framework for the full N-body problem in SE(3) and its reduction to the circular restricted full three-body problem," *Celestial Mechanics and Dynamical Astronomy*, Vol. 135, 2023. https://doi.org/10.1007/s10569-023-10156-1.
- [12] McCann, B. S., Anderson, A., Nazari, M., and Canales Garcia, D., "Circular restricted full three-body problem with rigid-body spacecraft dynamics in binary asteroid systems," *Celest Mech Dyn Astron*, Vol. 136, No. 9, 2024. https://doi.org/10.1007/s10569-024-10180-9.
- [13] Anderson, A., McCann, B. S., Canales Garcia, D., and Nazari, M., "Utilizing the Geometric Mechanics Framework to Predict Attitude in a Full Ephemeris Model of the Cislunar Region," *Communications in Nonlinear Science and Numerical Simulation*, 2023. https://doi.org/10.2139/ssrn.4569231.
- [14] Wittal, M., and Nazari, M., "Autonomous Constrained Control for Arbitrary Configurations for Gimbaling Thrusters in SE(3)," *AIAA/AAS Astrodynamics Specialist Conference*, 2023.

- [15] McCann, B. S., Fagetti, M., Nazari, M., Wittal, M. M., and Smith, J. D., "Mass property estimation on TSE(3) via unscented Kalman filter using RCS thrusters," *Acta Astronautica*, Vol. 223, 2024, pp. 462–480. https://doi.org/https://doi.org/10.1016/j.actaastro.2024.07.011.
- [16] Lee, T., Leok, M., and McClamroch, N. H., "Lie group variational integrators for the full body problem," *Computational Methods in Applied Mechanics and Engineering*, Vol. 196, No. 8, 2005, doi: 10.1016/j.cma.2007.01.017.
- [17] Seo, D., and Nazari, M., "Rigid body adaptive stabilization on the tangent bundle of the Lie groups," *AIAA Scitech 2019 Forum*, 2019, doi: 10.2514/6.2019-0653.
- [18] Bhat, S., and Bernstein, D., "A Topological Obstruction to Continuous Global Stabilization of Rotational Motion and the Unwinding Phenomenon," *Systems & Control Letters*, Vol. 39, 2000, pp. 63–70. https://doi.org/10.1016/S0167-6911(99)00090-0.
- [19] Sanyal, A., "Optimal Attitude Estimation and Filtering Without Using Local Coordinates Part I: Uncontrolled and Deterministic Attitude Dynamics," *American Control Conference*, 2005, pp. 5734–5739. https://doi.org/10.1109/ACC.2006.1657639.
- [20] Cao, L., and Li, H., "Unscented predictive variable structure filter for satellite attitude estimation with model errors when using low precision sensors," *Acta Astronautica*, Vol. 127, 2016, pp. 505–513. https://doi.org/10.1016/j.actaastro.2016.06.045.
- [21] Vandyke, M., Schwartz, J., and Hall, C., "Unscented Kalman Filtering for spacecraft attitude state and parameter estimation," *Advances in the Astronautical Sciences*, Vol. 119, 2004.
- [22] Markley, F. L., and Crassidis, J. L., Correction to: Fundamentals of Spacecraft Attitude Determination and Control, Springer, New York, 2014, isbn: 978-1-4939-0802-8.
- [23] Bohn, J., Sanyal, A. K., and Butcher, E., "Unscented state estimation for rigid body attitude motion with a finite-time stable observer," 2016 IEEE 55th Conference on Decision and Control, 2016, pp. 4698–4703. https://doi.org/10.1109/CDC.2016.7798985.
- [24] Brossard, M., Bonnabel, S., and Condomines, J., "Unscented Kalman filtering on Lie groups," *IEEE/RSJ International Conference on Intelligent Robots and Systems (IROS)*, 2017, doi: 10.1109/IROS.2017.8206066.
- [25] Brossard, M., Bonnabel, S., and Barrau, A., "Unscented Kalman filter on Lie groups for visual inertial odometry," "IEEE/RSJ International Conference on Intelligent Robots and Systems (IROS), 2018, doi: 10.1109/IROS.2018.8593627.
- [26] Wittal, M. M., McCann, B., Benavides, J., and Nazari, M., "Launch Vehicle Ambiguity Remediation and Morse-Lyapunov-Based Control with Parameter Uncertainties," *Journal of Spacecraft and Rockets*, 2025 (Submitted).
- [27] Dutta, S., Way, D., Zumwalt, C., and Blette, D., "Postflight Assessment of Mars 2020 Entry, Descent, and Landing Simulation," *Journal of Spacecraft and Rockets*, Vol. 0, No. 0, 0, pp. 1–11. https://doi.org/10.2514/1.A35771.
- [28] Lee, M., Shea, P., Pinier, J., and Chan, D., "Uncertainty Quantification of Artemis I Space Launch System Integrated Aerodynamics Databases," *Journal of Spacecraft and Rockets*, Vol. 0, No. 0, 0, pp. 1–10. https://doi.org/10.2514/1.A35844, URL https://doi.org/10.2514/1.A35844.

- [29] Wittal, M. M., Asher, B. W., McCann, B., and Nazari, M., "Autonomous Control for Arbitrary Thruster Configurations and Mass Properties in Special Euclidean Group SE(3)," 74th International Astronautical Congress, 2023.
- [30] Pagone, M., Novara, C., Martella, P., and Nocerino, C., "GNC robustness stability verification for an a, author = Arora, J.S., Elwakeil, O.A., Chahande, A.I. et al.utonomous lander," *Aerospace Science and Technology*, Vol. 100, 2020, p. 105831. https://doi.org/https://doi.org/10.1016/j.ast.2020.105831, URL https://www.sciencedirect.com/science/article/pii/S1270963819318413.
- [31] Arora, J., Elwakeil, O., Chahande, A., et al., "Global optimization methods for engineering applications: A review," *Structural Optimization*, No. 9, 1995, p. 137–159. https://doi.org/10.1007/BF01743964.
- [32] Deray, J. S. J., and Atchuthan, D., "A micro Lie theory for state estimation in robotics," 2018 arXiv preprint, 2018.
- [33] Sjøberg, A., and Egeland, O., "An EKF for Lie groups with application to crane load dynamics," *Modeling, Identification and Control: A Norwegian Research Bulletin*, Vol. 40, 2019, doi: 10.4173/mic.2019.2.3, pp. 109–124.
- [34] Sastry, S. S., Nonlinear Systems: Analysis, Stability, and Control, Springer, 1999.
- [35] Murray, R. M., Li, Z., and Sastry, S. S., A Mathematical Introduction to Robotic Manipulation, CRC Press, 1994.
- [36] Lee, D., and Vukovich, G., "Robust adaptive terminal sliding mode control on SE(3) for autonomous spacecraft rendezvous and docking," *Nonlinear Dynamics*, Vol. 83, 2016, doi: 10.1007/s11071-015-2479-1, pp. 2263–2279.
- [37] McCann, B. S., Wittal, M. M., and Nazari, M., "Relative Spacecraft Position and Attitude in the Circular Restricted Three-Body Problem: TSE(3) vs. Dual Quaternions," AIAA SCITECH 2023 Forum, 2023. https://doi.org/10.2514/6.2023-0698, URL https://arc.aiaa.org/doi/abs/10.2514/6.2023-0698.
- [38] Wittal, M. M., McCann, B., Benavides, J., and Nazari, M., "Ambiguity Remediation in Launch Vehicles with Parameter Uncertainties: A Comparison between Special Euclidean Group and Dual Quaternion," *AIAA/AAS Astrodynamics Specialist Conference*, Vol. 22-623, 2022.